



Unexpected decline in the ocean carbon sink under record-high sea surface temperatures in 2023

Received: 3 October 2024

Accepted: 16 June 2025

Published online: 2 September 2025

Jens Daniel Müller ¹, Nicolas Gruber ¹, Aline Schneuwly ¹, Dorothee C. E. Bakker ², Marion Gehlen ³, Luke Gregor ¹, Judith Hauck ^{4,5}, Peter Landschützer ⁶ & Galen A. McKinley ⁷

Check for updates

In 2023, sea surface temperatures (SSTs) reached record highs, partly due to a strong El Niño. Based on historical responses to elevated global mean SSTs, oceanic CO₂ uptake in 2023 should have increased ($-0.11 \pm 0.04 \text{ PgC yr}^{-1}$), driven by reduced outgassing in the tropical Pacific Ocean. However, using observation-based estimates of ocean CO₂ fugacity, we show here that the global non-polar ocean absorbed about 10% less CO₂ than expected ($+0.17 \pm 0.12 \text{ PgC yr}^{-1}$). This weakening was caused by the anomalous outgassing of CO₂ in the subtropical and subpolar regions, especially in the Northern Hemisphere, driven primarily by elevated SSTs reducing the solubility of CO₂. In most regions, this SST-induced outgassing was mitigated by the depletion of dissolved inorganic carbon in the surface mixed layer. Such negative feedbacks caused an overall muted response of the ocean carbon sink to the record-high SSTs, but this resilience may not persist under long-term warming or more severe SST extremes.

The ocean currently removes about a quarter of the annual anthropogenic CO₂ emissions from the atmosphere^{1–3}. However, how further global warming⁴ and the increasing occurrence of anomalously high sea surface temperatures (SSTs)^{5–7} might affect the functioning of this sink remains unclear. Given that most parts of the ocean experienced record-high SSTs in 2023^{8–10}, this particular year provides a unique opportunity to study this impact. Without global warming, this anomalous state of the surface ocean would have been virtually impossible¹¹. Even accounting for the linear trend in SSTs over the past 34 years, the annual mean anomaly of $+0.21 \pm 0.02^\circ\text{C}$ was the largest observed between 50°S and 65°N (Fig. 1a). In addition to global warming, a strong El Niño was an important contributor to this unprecedented SST anomaly^{8,10,12}. The spatial pattern of the SST anomalies represented in many parts the typical response to this phenomenon

(Fig. 1c), but unusually high temperatures in the North Atlantic Ocean made 2023 distinct^{13,14}.

It is well established that warming reduces the solubility of CO₂ in seawater, favouring increased outgassing of CO₂ to the atmosphere¹⁵. Under isochemical conditions, that is, when the dissolved inorganic carbon (DIC) concentration and alkalinity (TA) remain constant, each 1°C rise in temperature increases the fugacity of CO₂ ($f\text{CO}_2$) by ~4% (ref. 16). Thus, in the absence of any compensating mechanism, the 2023 SST anomaly of $+0.2^\circ\text{C}$ would have raised $f\text{CO}_2$ by 4 µatm. Such an increase in the oceanic $f\text{CO}_2$ would largely eliminate the mean sea-air $f\text{CO}_2$ gradient ($\Delta f\text{CO}_2$) over the non-polar global ocean¹⁷ and cause the uptake of CO₂ from the atmosphere to cease.

However, non-thermal processes, such as changes in ocean circulation, mixing and biogeochemical processes, can compensate for the

¹Environmental Physics, Institute of Biogeochemistry and Pollutant Dynamics, ETH Zurich, Zurich, Switzerland. ²Centre for Ocean and Atmospheric Sciences, School of Environmental Sciences, University of East Anglia, Norwich, UK. ³Laboratoire des Sciences du Climat et de l'Environnement, LSCE-IPSL, CEA-CNRS-UVSQ, Université Paris-Saclay, Gif-sur-Yvette, France. ⁴Alfred-Wegener-Institut, Helmholtz-Zentrum für Polar- und Meeresforschung, Bremerhaven, Germany. ⁵Universität Bremen, Bremen, Germany. ⁶Flanders Marine Institute (VLIZ), Ostend, Belgium. ⁷Columbia University and Lamont-Doherty Earth Observatory, Palisades, NY, USA. e-mail: jensdaniel.mueller@usys.ethz.ch

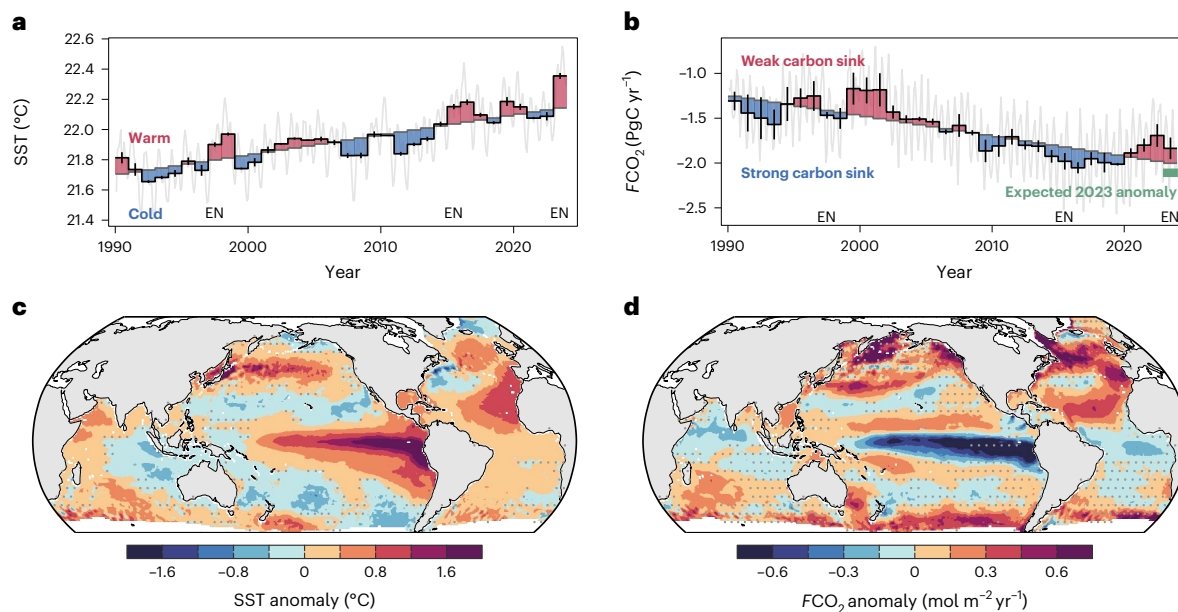


Fig. 1 | Diagnosis of the record-high SSTs in 2023 and their impact on sea-to-air CO₂ fluxes. **a, b**, Time series of mean SSTs (**a**) and fCO₂ (**b**) over the region between 50° S and 65° N based on the ensemble mean of four fCO₂ products (Extended Data Table 1). Annual (black lines) and monthly mean (grey lines) values are shown. Annual mean anomalies relative to the linear long-term trend from 1990 to 2022, representing the baseline of our analysis, are shaded in red and blue (the meaning of the shading is indicated in the respective panel). Error bars indicate the standard deviation of the annual anomalies across the four fCO₂ products (the annual anomalies for each fCO₂ product are shown individually in Supplementary Fig. 1). EN indicates years with a strong El Niño. In **b**, the green bar for 2023 indicates the fCO₂ range expected from the linear relationship between global mean fCO₂ and SST anomalies between 1990 and 2022 (see ‘Expected fCO₂ anomaly in 2023’ in Methods). **c, d**, Maps of the SST (**c**) and fCO₂ (**d**) anomalies for 2023 relative to the extrapolated long-term trend. Stippling indicates regions where the ensemble standard deviation is higher than the absolute anomaly.

products (the annual anomalies for each fCO₂ product are shown individually in Supplementary Fig. 1). EN indicates years with a strong El Niño. In **b**, the green bar for 2023 indicates the fCO₂ range expected from the linear relationship between global mean fCO₂ and SST anomalies between 1990 and 2022 (see ‘Expected fCO₂ anomaly in 2023’ in Methods). **c, d**, Maps of the SST (**c**) and fCO₂ (**d**) anomalies for 2023 relative to the extrapolated long-term trend. Stippling indicates regions where the ensemble standard deviation is higher than the absolute anomaly.

SST-driven (thermal) effects by modifying the DIC and TA concentrations¹⁸. Thermal and non-thermal drivers are often in a delicate balance, which is well documented for the seasonal cycle of surface ocean fCO₂ (refs. 16,19,20). In some cases, non-thermal processes even overcompensate the direct temperature effect. This was observed during previous El Niño years, when the oceanic uptake of CO₂ became unusually strong (Fig. 1a) despite anomalously high global SSTs. This strengthening during El Niño results from the reduced outgassing of CO₂ in the eastern equatorial Pacific Ocean of roughly -0.1 to -0.2 PgC yr⁻¹ due to reduced upwelling of cold and CO₂-rich waters²¹. Note that here we report sea-to-air CO₂ fluxes: an (anomalous) oceanic CO₂ uptake is negative and outgassing is positive. In contrast, fCO₂ in the subtropics tends to be thermally controlled, so that exceptionally warm SSTs are associated with enhanced outgassing of CO₂ (refs. 22–24). Hence, the overall response of the ocean carbon sink to unusual warming depends sensitively on the regional distribution of the SST anomalies and the outcome of the ‘tug of war’ between the thermal and non-thermal drivers of the surface ocean carbon cycle.

To quantify the impact of 2023’s record-high SSTs on the oceanic uptake of CO₂, we employed four observation-based fCO₂ products^{25–29}. These products are machine learning-based statistical models that were first trained on in situ fCO₂ observations and then used to produce gap-filled maps of the evolution of surface ocean fCO₂ based on remotely sensed predictor variables. Our main results were obtained with fCO₂ products trained on version 2024 of the Surface Ocean CO₂ Atlas (SOCAT) providing observations through December 2023³⁰. From the mapped fCO₂ fields, we computed the sea-to-air CO₂ flux (fCO₂) as the product of ΔfCO_2 , the wind-dependent gas transfer velocity (k_w) and the solubility of CO₂ in seawater (K_0 ; see Methods). In addition, we provide in Supplementary Figs. 14 and 15 the originally submitted near-real-time (NRT) estimates obtained from the same four fCO₂ products trained on observations available only through 2022, but still used to predict surface ocean fCO₂ through the end of 2023. These NRT estimates were initially validated through a prediction skill assessment

based on truncated training data and comparisons with individual fCO₂ observations from 2023 (Supplementary Information)^{30–33} and overall agree well with the updated estimates. Furthermore, we employed hindcast simulations from two global ocean biogeochemical models (GOBMs)^{29,34,35}, physically forced with reanalysis data³⁶, to explore how physical and biogeochemical anomalies in the ocean interior shape the surface anomalies.

We focused primarily on the low and middle latitudes between -50° S and -65° N, referred to as the global non-polar ocean. This region covers $>90\%$ of the global non-sea-ice-covered ocean surface. The Arctic and polar and subpolar biomes of the Southern Ocean are excluded from the discussion because data sparsity leads to higher uncertainties in the flux anomaly estimates, as evidenced by the substantially larger spread across the four fCO₂ products. However, we still report the anomalies and associated uncertainties for these high-latitude regions (Table 1 and Extended Data Figs. 3 and 4).

Impact of record-high SSTs on the oceanic CO₂ uptake

The four observation-based fCO₂ products infer for 2023 an anomalous weakening of the ocean carbon sink by $+0.17 \pm 0.12$ PgC yr⁻¹ integrated over the global non-polar analysis region (Fig. 1b,d and Table 1). This flux anomaly corresponds to a roughly 10% reduction in CO₂ uptake relative to a baseline estimate that accounts for the linear trend from 1990 through 2022 (Fig. 1b and Methods), reflecting the expected increase in the uptake of CO₂ due to rising atmospheric CO₂ (ref. 2). The magnitude of the decline in ocean carbon uptake in 2023 is not unprecedented over the past 34 years, but it is unusual in a year with record-high SSTs exceeding $+0.2^\circ$ C (Fig. 2a). In fact, a decline in the ocean carbon sink has not occurred before in years with an annual mean SST anomaly in excess of $+0.1^\circ$ C. Based on the (largely El Niño-driven) relationship between annual mean anomalies in SSTs and oceanic CO₂ uptake over the global non-polar ocean (Fig. 2a), an anomalously strong uptake of -0.11 ± 0.04 PgC yr⁻¹ could have been expected in 2023 (Figs. 1b and 2a).

Table 1 | Annual mean $f\text{CO}_2$ and SSTs in 2023 together with the respective anomalies relative to a linear trend baseline

Region	Biome	SST ($^{\circ}\text{C}$)		$f\text{CO}_2$ ($\text{mol m}^{-2} \text{yr}^{-1}$)		$f\text{CO}_2$ (Pg yr^{-1})	
		Absolute	Anomaly	Absolute	Anomaly	Absolute	Anomaly
North Atlantic	SPSS	+8.69 \pm 0.06	+0.10 \pm 0.03	-2.49 \pm 0.06	+0.31 \pm 0.17	-0.28 \pm 0.02	+0.03 \pm 0.02
	STSS	+19.01 \pm 0.03	+0.26 \pm 0.03	-2.03 \pm 0.08	+0.26 \pm 0.11	-0.15 \pm 0	+0.02 \pm 0.01
	STPS	+26.01 \pm 0.06	+0.50 \pm 0.05	-0.18 \pm 0.03	+0.16 \pm 0.02	-0.05 \pm 0.01	+0.04 \pm 0.01
	Total	+20.61 \pm 0.03	+0.36 \pm 0.02	-1.05 \pm 0.03	+0.21 \pm 0.07	-0.47 \pm 0.02	+0.10 \pm 0.03
North Pacific	SPSS	+8.86 \pm 0.07	+0.37 \pm 0.04	-1.03 \pm 0.21	+0.30 \pm 0.34	-0.17 \pm 0.04	+0.05 \pm 0.06
	STSS	+19.46 \pm 0.03	+0.41 \pm 0.04	-2.22 \pm 0.14	+0.22 \pm 0.05	-0.21 \pm 0.01	+0.02 \pm 0.01
	STPS	+26.01 \pm 0.03	0 \pm 0.02	-0.40 \pm 0.02	+0.06 \pm 0.02	-0.21 \pm 0.01	+0.03 \pm 0.01
	Total	+21.49 \pm 0.01	+0.13 \pm 0.01	-0.76 \pm 0.06	+0.13 \pm 0.09	-0.60 \pm 0.05	+0.10 \pm 0.07
Northern Hemisphere extratropics		+21.17 \pm 0.02	+0.21 \pm 0.01	-0.86 \pm 0.05	+0.16 \pm 0.08	-1.07 \pm 0.06	+0.19 \pm 0.1
Tropics	PEQU-E	+27.45 \pm 0.08	+1.24 \pm 0.07	+1.48 \pm 0.29	-0.51 \pm 0.35	+0.27 \pm 0.05	-0.09 \pm 0.06
	PEQU-W	+29.57 \pm 0.07	+0.04 \pm 0.03	+0.21 \pm 0.02	+0.03 \pm 0.04	+0.03 \pm 0	0 \pm 0.01
	AEQU	+27.56 \pm 0.03	+0.27 \pm 0.08	+0.22 \pm 0.14	-0.09 \pm 0.06	+0.02 \pm 0.01	-0.01 \pm 0.01
	Equ. Ind.	+28.31 \pm 0.03	+0.02 \pm 0.05	+0.27 \pm 0.10	-0.04 \pm 0.03	+0.09 \pm 0.04	-0.01 \pm 0.01
	Total	+28.28 \pm 0.04	+0.34 \pm 0.03	+0.53 \pm 0.08	-0.14 \pm 0.07	+0.41 \pm 0.06	-0.11 \pm 0.05
Southern Hemisphere extratropics	SA-STPS	+22.93 \pm 0.03	+0.11 \pm 0.04	-0.13 \pm 0.10	0 \pm 0.08	-0.03 \pm 0.02	0 \pm 0.02
	SP-STPS	+22.29 \pm 0.03	+0.11 \pm 0.03	-0.33 \pm 0.05	0 \pm 0.04	-0.22 \pm 0.04	0 \pm 0.03
	South. Ind.	+22.35 \pm 0.03	+0.09 \pm 0.09	-1.20 \pm 0.05	+0.10 \pm 0.06	-0.25 \pm 0.01	+0.02 \pm 0.01
	SO-STSS	+13.15 \pm 0.03	+0.25 \pm 0.05	-1.96 \pm 0.16	+0.18 \pm 0.18	-0.69 \pm 0.06	+0.06 \pm 0.06
	Total	+20.19 \pm 0.02	+0.14 \pm 0.04	-0.81 \pm 0.07	+0.06 \pm 0.08	-1.18 \pm 0.10	+0.08 \pm 0.11
Global non-polar		+22.35 \pm 0.01	+0.21 \pm 0.02	-0.53 \pm 0.02	+0.05 \pm 0.04	-1.84 \pm 0.08	+0.17 \pm 0.12
Polar	SO-SPSS	+3.84 \pm 0.11	+0.13 \pm 0.03	+0.07 \pm 0.40	+0.26 \pm 0.28	+0.02 \pm 0.15	+0.10 \pm 0.10
	SO-ICE	-0.95 \pm 0.07	+0.08 \pm 0.03	-0.16 \pm 0.09	+0.26 \pm 0.14	-0.04 \pm 0.03	+0.05 \pm 0.03
	Arctic	-0.16 \pm 0.43	-0.08 \pm 0.09	-1.47 \pm 0.60	+0.26 \pm 0.05	-0.14 \pm 0.02	+0.03 \pm 0.01
Global		+18.73 \pm 0.02	+0.19 \pm 0.01	-0.49 \pm 0.07	+0.09 \pm 0.06	-1.99 \pm 0.25	+0.34 \pm 0.25

SST estimates are regional averages ($^{\circ}\text{C}$), whereas $f\text{CO}_2$ estimates are given both as regional integrals (Pg C yr^{-1}) and averages ($\text{mol m}^{-2} \text{yr}^{-1}$). All estimates represent the mean \pm standard deviation over four observation-based $f\text{CO}_2$ products. The anomaly estimates in this table are also presented in Extended Data Fig. 4. The biomes are designated according to the map shown in Extended Data Fig. 2: SPSS, subpolar seasonally stratified; STSS, subtropical seasonally stratified; STPS, subtropical permanently stratified; PEQU-E, eastern equatorial Pacific; PEQU-W, western equatorial Pacific; AEQU, tropical Atlantic; Equ. Ind., tropical Indian Ocean; SA, South Atlantic; SP, South Pacific; South. Ind., southern Indian Ocean; SO, Southern Ocean; ICE, marginal sea ice.

Compared with this expectation, the actual CO_2 uptake was $0.27 \pm 0.13 \text{ Pg C yr}^{-1}$ weaker. Thus, something was different in 2023 compared with in previous exceptionally warm years.

The exceptional reduction in uptake in 2023 was not caused by the eastern equatorial Pacific (PEQU-E) biome. In fact, this biome actually experienced reduced outgassing of CO_2 by $-0.09 \pm 0.06 \text{ Pg C yr}^{-1}$, that is, an anomalous uptake, which is consistent with the expectation based on the 2023 SST anomaly (Fig. 2d) and matches the response to previous El Niño events^{21,37,38}. Slightly reinforced by reduced CO_2 outgassing from the tropical Atlantic and Indian oceans (Fig. 1d), the flux anomalies integrated over the global tropics amounted to $-0.11 \pm 0.05 \text{ Pg C yr}^{-1}$ (Table 1), which closely matches the expected uptake anomaly for the global ocean (Fig. 1b).

Hence, the decline in the uptake of CO_2 must have occurred entirely in the extratropical ocean. Here, widespread positive SST anomalies, especially in the Northern Hemisphere (Fig. 1c), triggered an anomalous outgassing of CO_2 (Table 1) that was stronger than in previous years, especially those affected by El Niño (Supplementary Fig. 7).

Among the extratropical regions, the North Atlantic experienced the highest, most persistent and extensive SST anomalies in 2023. In particular, the North Atlantic subtropical permanently stratified (NA-STPS) biome (see the biome map in Extended Data Fig. 2) faced an unprecedented annual mean SST anomaly of $+0.50 \pm 0.05 ^{\circ}\text{C}$, which caused a substantial decline in the CO_2 uptake by $+0.04 \pm 0.01 \text{ Pg C yr}^{-1}$ (Table 1). This response fits the historic relationship between CO_2

flux and SST anomalies very well (Fig. 2c), although the SST anomaly exceeds the previous record over the past 34 years by more than 50%. The North Atlantic subpolar seasonally stratified (NA-SPSS) and subtropical seasonally stratified (NA-STSS) biomes experienced even stronger CO_2 flux density anomalies. They exceed those in the NA-STPS (Table 1) and are stronger than expected from the annual mean SST anomalies (Extended Data Fig. 1). However, the integrated CO_2 flux anomalies in the two seasonally stratified biomes are lower than in the STPS biome due to their smaller surface area. In total, the North Atlantic contributed a flux anomaly of $+0.10 \pm 0.03 \text{ Pg C yr}^{-1}$.

In 2023, the CO_2 uptake also weakened in all biomes of the North Pacific (Table 1). The strongest anomalous outgassing per surface area occurred in the two smaller biomes of the North Pacific (NP-STSS and NP-SPSS), but all biomes jointly contributed $+0.10 \pm 0.07 \text{ Pg C yr}^{-1}$ to the weakening of the global ocean carbon sink (Fig. 1d and Table 1). These flux anomalies were substantially stronger than expected from past responses to SST anomalies alone (Extended Data Fig. 1).

The STPS biomes of the Southern Hemisphere revealed overall weak CO_2 flux anomalies in 2023. Even though all three basins showed a positive SST anomaly, only the Indian Ocean STPS biome showed anomalous outgassing (Table 1). Considering also the STSS biome of the Southern Ocean, the Southern Hemisphere extratropics contributed in total $+0.08 \pm 0.11 \text{ Pg C yr}^{-1}$ to the global flux anomaly.

In the above analysis, we formally quantified the uncertainty of our estimates as the standard deviation across the four observation-based

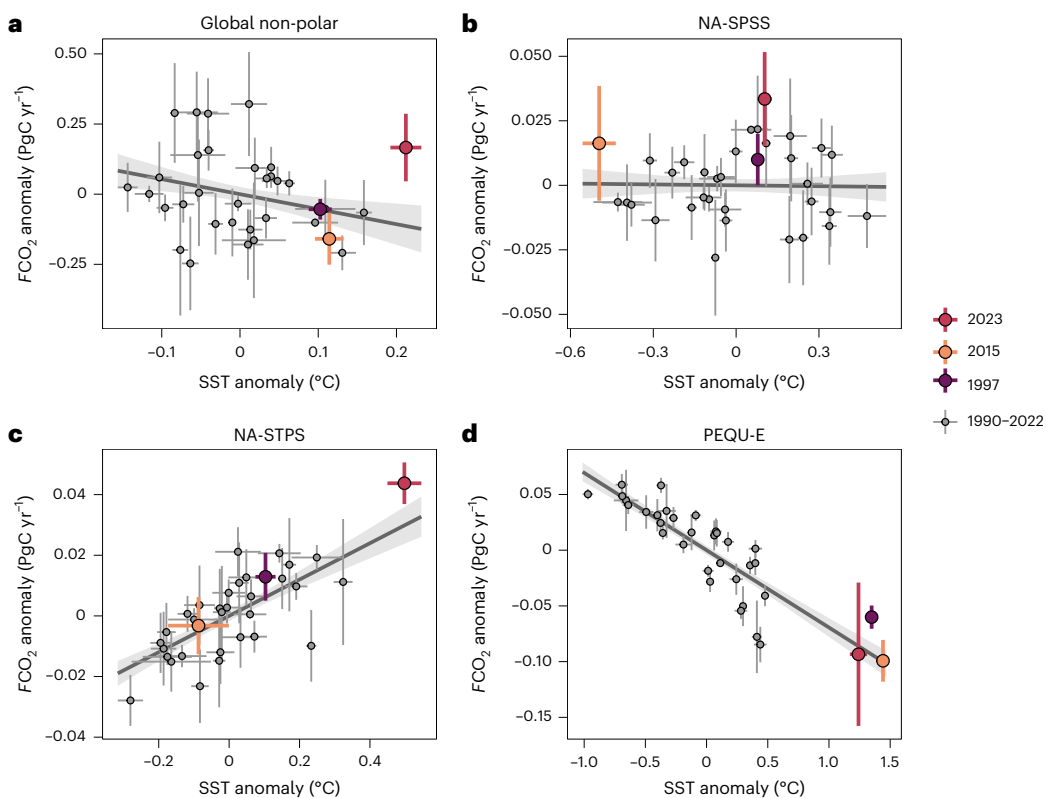


Fig. 2 | Relationship between annual mean SST and $f\text{CO}_2$ anomalies from 1990 to 2023. **a–d**, All SST and $f\text{CO}_2$ anomalies were determined relative to a linear long-term trend and are shown for the global non-polar ocean (**a**), NA-SPSS (**b**), NA-STPS (**c**) and PEQU-E (**d**). Symbols and error bars represent the mean and standard deviation across the ensemble of four observation-based $f\text{CO}_2$

products, respectively. The El Niño years 1997, 2015 and 2023 are highlighted by warm colours. The grey lines and ribbons indicate linear regressions and 68% confidence intervals, respectively, across all annual mean anomalies from 1990 to 2022. A biome map and correlation plots for other biomes are presented in Extended Data Figs. 2 and 3, respectively.

$f\text{CO}_2$ products. At the regional scale, we have high confidence in our estimates for the tropical and subtropical biomes of the Northern Hemisphere, given that the $f\text{CO}_2$ products agree in sign and magnitude (Table 1 and Extended Data Fig. 4). Due to the larger spread in the subpolar biomes of the Northern and Southern hemispheres, we assign only medium confidence to these estimates. Estimates for the non-polar global ocean (Table 1 and Extended Data Fig. 4) range from a very minor strengthening of the sink (OceanSODA) to a strong weakening by $+0.27 \text{ PgC yr}^{-1}$ (SOM-FFN). As the $f\text{CO}_2$ products agree (mostly) in sign but not in magnitude, we assign a medium confidence to our estimate for the non-polar global ocean ($+0.17 \pm 0.12 \text{ PgC yr}^{-1}$). However, when compared against the expectation of an anomalous strengthening of the sink ($-0.11 \pm 0.04 \text{ PgC yr}^{-1}$) instead of the zero flux anomaly at the baseline (Fig. 1b), the consistency of estimates is higher. Hence, we have high confidence in our conclusion that the ocean carbon sink in 2023 was indeed weaker ($+0.27 \pm 0.13 \text{ PgC yr}^{-1}$) than expected based on the long-term trend and the global annual mean SST anomaly. The overall confidence in our estimates is further supported by an almost identical mean estimate of the global non-polar CO_2 flux anomaly based on the NRT version of our $f\text{CO}_2$ products ($+0.16 \pm 0.28 \text{ PgC yr}^{-1}$), as well as highly consistent spatial patterns in the flux anomalies (Supplementary Fig. 14), except for the STSS biome in the South Atlantic.

Driver attribution and seasonality of CO_2 flux anomalies

The annual mean CO_2 flux anomaly over the non-polar global ocean in 2023 was primarily (>95%) driven by anomalies in $\Delta f\text{CO}_2$ (Fig. 3a and Extended Data Fig. 5). The $\Delta f\text{CO}_2$ anomaly triggered positive CO_2 flux anomalies (that is, a weaker sink) in all regions that experienced a positive SST anomaly, except in PEQU-E (Figs. 1c and 3a). Anomalies

in wind speed further modulated the annual mean CO_2 flux at regional scales (Fig. 3b), for example, in PEQU-E or the North Pacific off Japan (NP-STSS), but they had a small net impact on globally integrated fluxes (Extended Data Fig. 5). The modulation of $\Delta f\text{CO}_2$ -driven flux anomalies through wind anomalies (that is, the cross term $\Delta f\text{CO}_2 \times k_w K_0$) was negligible (Fig. 3c and Extended Data Fig. 5) and will not be discussed further.

To quantify the causes of the 2023 anomalies in $\Delta f\text{CO}_2$, we further decomposed the main contributor, the oceanic $f\text{CO}_2$ anomaly, into thermal and non-thermal components (see Methods). The regions with the strongest SST anomalies revealed, by definition, the largest thermal component of the $f\text{CO}_2$ anomaly, that is, PEQU-E, the subpolar North Pacific and subtropical North Atlantic (Fig. 3d). These regions also experienced the strongest non-thermal component (Fig. 3e). Hence, the resulting total $f\text{CO}_2$ anomaly remained comparably small at regional scales (Fig. 3f) and was slightly positive ($+0.3 \pm 0.9 \mu\text{atm}$) when averaged over the global non-polar ocean weighted by the surface area and $k_w K_0$ (Extended Data Fig. 6).

To delve further into the attribution of the 2023 CO_2 flux anomalies, we compared their seasonal evolution and drivers for three characteristic biomes with robust anomaly estimates, namely, PEQU-E, NA-STPS and NA-SPSS. For this attribution analysis, we further corroborated the observation-based surface anomalies with simulations from two GOBMs that permit us to connect the processes at the surface with those occurring at depth (see Methods). The GOBM simulations showed a similar seasonal evolution of the SST and CO_2 flux anomalies in 2023 as our observation-based estimates (Fig. 4 and Extended Data Fig. 7) and are therefore considered reliable tools to interpret the underlying physical and biogeochemical processes.

The seasonal evolution in 2023 of SST anomalies in PEQU-E resembles that of previous El Niño events. A positive SST anomaly of around

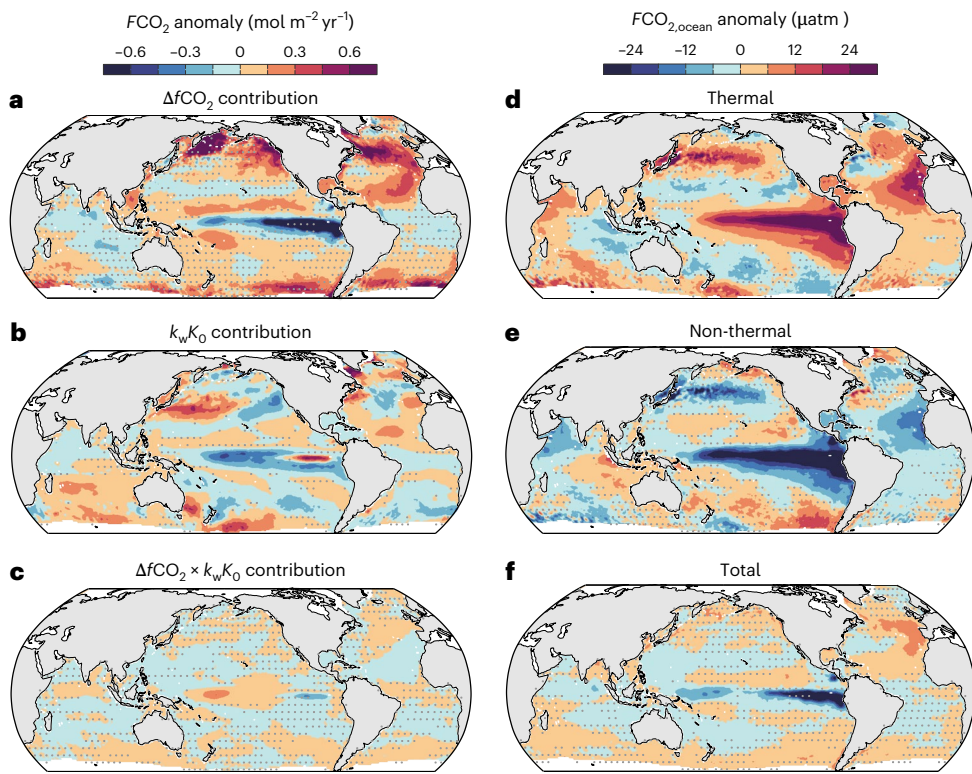


Fig. 3 | Attribution of 2023 annual mean CO_2 flux anomalies and oceanic $f\text{CO}_2$ decomposition. **a–c**, Attribution of CO_2 flux anomalies to their primary drivers, that is, the CO_2 fugacity gradient between ocean and atmosphere ($\Delta f\text{CO}_2$) (a), the product of the gas transfer velocity and the solubility of CO_2 (k_wK_0), which

is primarily controlled by wind speed (b), and the cross product of both drivers ($\Delta f\text{CO}_2 \times k_wK_0$) (c). **d–f**, Decomposition of the total oceanic $f\text{CO}_2$ anomalies (f) into thermal (d) and non-thermal (e) components. Stippling indicates regions where the ensemble standard deviation is higher than the absolute ensemble mean.

2 °C established gradually over the first half of 2023 and remained stable thereafter (Fig. 4b, right). This SST evolution was mirrored by a reduction in the outgassing of CO_2 (that is, a growing sink) by up to $0.8 \text{ mol m}^{-2} \text{ yr}^{-1}$ in the $f\text{CO}_2$ products and $0.2 \text{ mol m}^{-2} \text{ yr}^{-1}$ in the GOBMs. The reduced outgassing was primarily a consequence of negative $\Delta f\text{CO}_2$ anomalies, but was reinforced by anomalously low wind speeds. The negative $\Delta f\text{CO}_2$ anomalies in PEQU-E resulted from reduced upwelling of remineralized DIC. To quantify this well-known non-thermal driver, we used GOBM simulations and subtracted the salinity-normalized TA (sTA) anomaly from the salinity-normalized DIC (sDIC) anomaly. We then converted the anomalous decline in sDIC – sTA ($-25 \mu\text{mol kg}^{-1}$; Fig. 4c, right) into an equivalent $f\text{CO}_2$ reduction of about $50 \mu\text{atm}$ (see Methods). This DIC-driven $f\text{CO}_2$ reduction is already partly compensated by the reduced outgassing of CO_2 over the course of 2023, but it still remains substantially stronger than the SST-driven increase in $f\text{CO}_2$ of $-30 \mu\text{atm}$ at the end of the year. Hence, the non-thermal component clearly won the ‘tug of war’ in PEQU-E.

In NA-SPSS, the monthly SST anomalies peaked in the summer at around $+1^\circ\text{C}$ and remained well above the range of past anomalies for the remainder of 2023. In contrast to PEQU-E, the resulting CO_2 flux anomaly in NA-SPSS was positive, that is, the CO_2 uptake in winter weakened and the outgassing in summer became stronger. This anomalous outgassing was found in both the $f\text{CO}_2$ products and GOBMs. This can be attributed to thermally driven $\Delta f\text{CO}_2$ anomalies (Fig. 4a, centre and Extended Data Figs. 5 and 6) and was slightly enhanced by weak winds that further reduced the CO_2 uptake from January to April (Extended Data Fig. 7). The mixed layer depth simulated by the GOBMs was anomalously shallow in 2023, suggesting increased stratification and reduced mixing of remineralized DIC into the surface layer (Extended Data Fig. 8). However, the simulated surface sDIC – sTA anomaly of $-3 \mu\text{mol kg}^{-1}$ in NA-SPSS was much weaker than in PEQU-E. This anomaly was established primarily in the summer, when the surface CO_2 flux anomalies were also strongest (Fig. 4a, centre). Integrated over the

summertime mixed layer depth of $\sim 50 \text{ m}$, the sDIC – sTA inventory decreased by roughly 0.15 mol m^{-2} over the course of 2023 (Fig. 4c, centre), which is almost identical to the cumulative CO_2 flux anomaly. This suggests that the surface CO_2 flux anomaly was the primary driver of the inventory anomaly in the surface mixed layer. Hence, the reduced mixing of DIC into the surface layer due to the increased stratification was either negligibly small or nearly balanced by a reduced primary production of organic matter (Extended Data Fig. 8). Overall, the thermal driver won the ‘tug of war’ and determined the CO_2 flux anomalies during the onset of the SST anomaly in NA-SPSS.

In NA-SPSS, the monthly peak SST anomalies were about as high as in NA-SPSS, but more confined to the summer months and less exceptional compared with the variability in previous decades (Fig. 4a, left). Similarly, the model- and observation-based CO_2 flux anomalies were less exceptional compared with previous years (Fig. 2), albeit more intense than in NA-SPSS (Fig. 4a, left). In contrast to NA-SPSS, wind anomalies played a more important role in regulating the 2023 CO_2 fluxes in NA-SPSS (Extended Data Figs. 5 and 7). Strong winds until May favoured the natural CO_2 sink, whereas weak winds throughout the rest of 2023 reduced the natural sink and thereby reinforced the anomalous outgassing triggered by positive $\Delta f\text{CO}_2$ anomalies. The interpretation of the GOBM simulations in the NA-SPSS biome is rather complex. The simulated increase in the summertime temperature was confined to a very shallow surface layer (10–20 m). This increase in temperature in the GOBMs is very similar to those seen in the $f\text{CO}_2$ products and hence induced a similar thermal $f\text{CO}_2$ anomaly. However, it triggered a higher $\Delta f\text{CO}_2$ anomaly because the compensating non-thermal $f\text{CO}_2$ anomaly simulated with the GOBMs is weaker than that diagnosed by the $f\text{CO}_2$ products (Extended Data Fig. 7). This difference can probably be attributed to an underestimation of the non-thermal $f\text{CO}_2$ component by the GOBMs²⁰ in the NA-SPSS biome, as previously documented for the seasonal cycle²⁰.

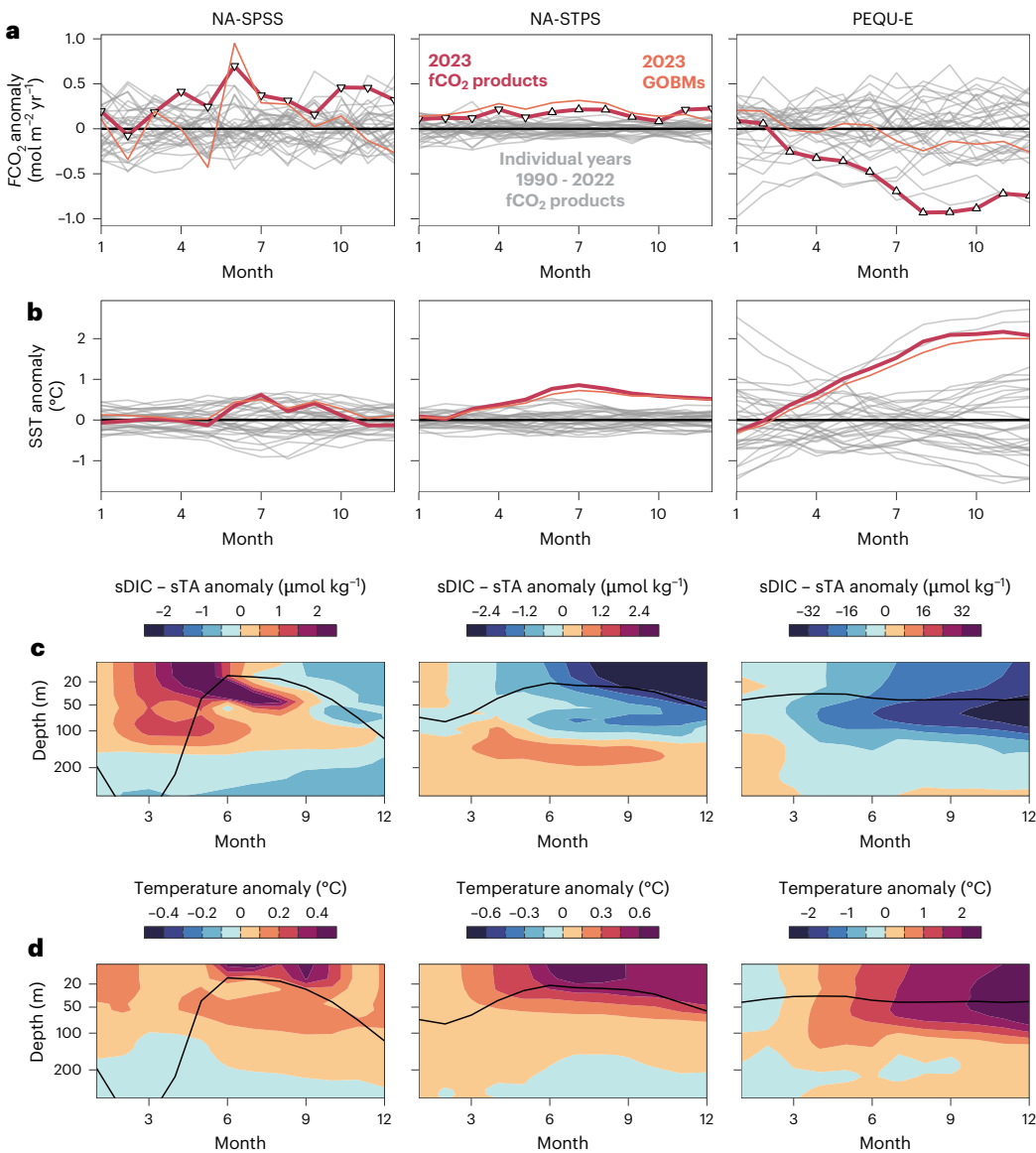


Fig. 4 | Modelled and observation-based seasonal evolution of surface and interior ocean properties for three key biomes. **a,b.** Monthly mean surface anomalies of the CO_2 flux density (**a**) and SST (**b**) in the NA-SPSS (left), NA-STPS (middle) and PEQU-E (right) biomes. The red and grey lines represent the fCO_2 product ensemble mean for 2023 and individual years 1990–2022, respectively; the orange lines represent the GOBM ensemble mean for 2023. In **a**, the triangles indicate the direction of the prevailing absolute CO_2 flux into (downwards) or out of (upwards) the ocean. **c,d.** Model simulations of the vertical mean monthly

anomalies of $\text{sDIC} - \text{sTA}$ (**c**) and temperature (**d**) in the NA-SPSS (left), NA-STPS (middle) and PEQU-E (right) biomes. In **c**, sDIC anomalies are adjusted for the sTA anomaly to capture the sDIC anomaly that is directly linked to fCO_2 anomalies. The $\text{sDIC} - \text{sTA}$ anomalies are presented as changes since January 2023 to remove legacy anomalies from 2022 and to allow direct comparison with the instantaneous surface flux anomalies. The black lines indicate the mean mixed layer depth. All vertical anomalies represent the mean of the two GOBMs.

Discussion

We have demonstrated that widespread record-high SSTs led to a reduction in the ocean carbon sink in 2023 compared with a linearly increasing baseline estimate. This reduction was unexpected considering the strengthening of the sink during previous unusually warm years, all characterized by El Niño conditions. To confirm this finding, we derived a first alternative estimate of the expected sink strength that is based on the actual spatial distribution of the SST anomalies in 2023 and the regional response of the air–sea CO_2 fluxes in previous decades ($-0.10 \pm 0.02 \text{ PgC yr}^{-1}$; Extended Data Fig. 1a,b), and a second alternative estimate that predicts the sink strength with a multiple linear regression model that considers as predictor variables the concentration and growth rate of atmospheric CO_2 and an El Niño index based on the SST anomalies in the equatorial Pacific ($-0.21 \pm 0.07 \text{ PgC yr}^{-1}$; Extended Data Fig. 1c). All three alternatives agree in that the ocean carbon sink should have

strengthened in 2023. The reason for the unexpected decline of the ocean carbon sink is the overcompensation of an anticipated anomalous CO_2 uptake in the tropics by an increase in CO_2 outgassing from the non-polar extratropics (Fig. 5b). Among these regions, the anomalous CO_2 outgassing in the subtropical North Atlantic, driven by unusually strong and persistent SST anomalies (Fig. 5a), stands out as a strong and robust feature.

Interestingly, the depletion of DIC in the NA-STPS biome by the end of 2023, reflected by the $\text{sDIC} - \text{sTA}$ anomaly of $-3 \mu\text{mol kg}^{-1}$ (Fig. 4b, centre), had an effect on surface ocean fCO_2 ($-5 \mu\text{atm}$) that was similar in magnitude but opposite in direction to that caused by the SST anomaly ($+0.5^\circ\text{C}$). This suggests that, by the end of the year, the DIC depletion fully compensated the thermal driver. The resulting decline in the anomalous outgassing towards winter is evident in our GOBM simulations, but less so in the observation-based fCO_2 products (Fig. 4a, centre).

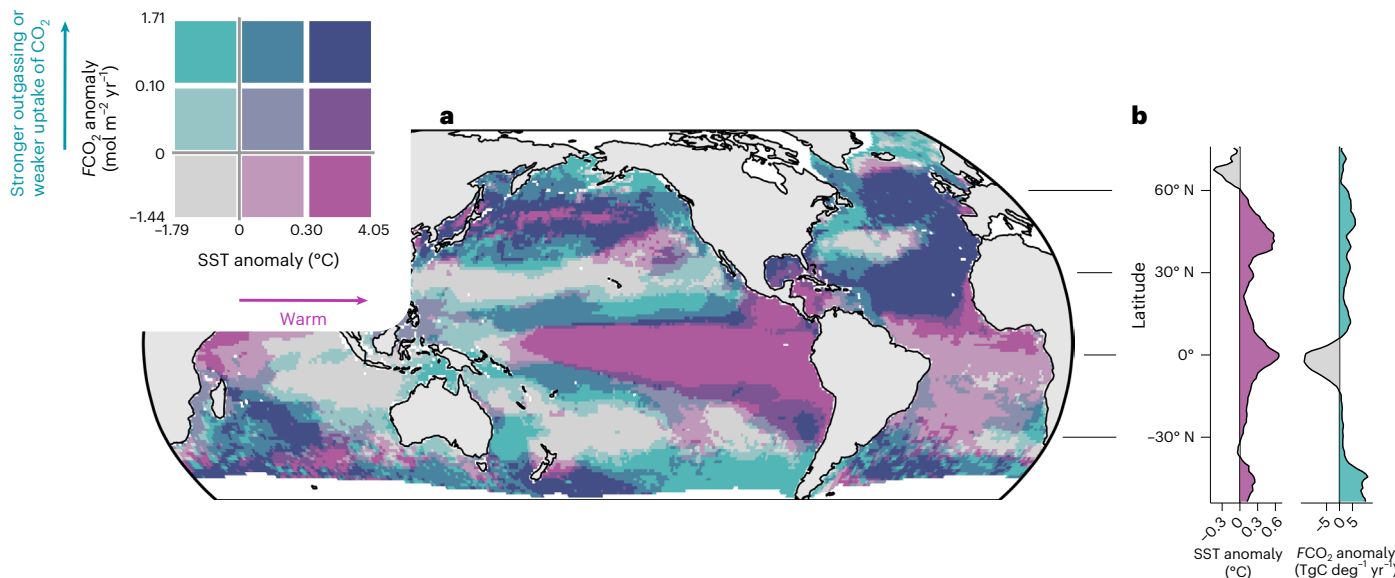


Fig. 5 | Annual mean anomalies in $f\text{CO}_2$ and the corresponding SST anomalies for 2023. **a**, Bivariate map of $f\text{CO}_2$ and SST anomalies. **b**, Zonal mean SST anomalies and zonally integrated $f\text{CO}_2$ anomalies, adapting the colour scale

from **a** to highlight latitudes with anomalously high (pink) or low (grey) SSTs and a weak (turquoise) or strong (grey) CO_2 uptake. All estimates are based on the ensemble mean of four $f\text{CO}_2$ products.

In contrast to the near balance of the thermal and non-thermal drivers in the NA-STPS biome, the non-thermal DIC anomaly remained dominant in PEQU-E by the end of 2023. Here, the integrated anomaly of $\text{sDIC} - \text{sTA}$ over the top 100 m had reached -2 mol m^{-2} , far exceeding the CO_2 flux anomaly of about -0.1 mol m^{-2} that occurred cumulatively over the course of the year (Fig. 4, right).

Using the anomalous state of the ocean by the end of 2023 to forecast the proceeding CO_2 flux anomalies, the expectation is that the anomalous outgassing in NA-STPS might have ceased, despite the continued elevated SSTs, provided that the DIC depletion remained during the first half of 2024. However, mixing during the boreal winter-time of 2023–2024 might have replenished the surface DIC pool. Hence, we expect a neutral to a reduced sink strength in NA-STPS in the first half of 2024. In PEQU-E, the remaining negative DIC anomaly favours continued reduced outgassing, provided that these water masses stay in contact with the atmosphere. However, as SST anomalies in PEQU-E decreased during the first half of 2024, CO_2 outgassing in this biome most probably returned to normal levels and we expect a rather neutral sink strength in PEQU-E in the first half of 2024. If indeed the reduced outgassing in the tropics faded out while the extratropics remained anomalously warm, the global ocean carbon sink might have continued to be in weak in early 2024.

Whether these projected CO_2 flux anomalies materialized in 2024 remains to be confirmed, ultimately through $f\text{CO}_2$ observations. A more immediate opportunity to quantify the oceanic CO_2 uptake in 2024 emerges from the possibility to predict the observation-based $f\text{CO}_2$ products^{25–28} that were trained on *in situ* $f\text{CO}_2$ observations through December 2023³⁰ for 1 year beyond the training data using the observed predictor fields already available for 2024. In fact, this study was originally conducted with such NRT predictions for 2023, and the similarity of the ensemble mean $f\text{CO}_2$ anomalies, as well as a thorough prediction skill assessment based on truncated training data (Supplementary Figs. 8–13), indicate that this approach is suitable for quantifying CO_2 flux anomalies with low latency.

The limitation of thermally induced CO_2 outgassing by DIC depletion that we observed for the 2023 warming event is crucial when considering the long-term response of the ocean carbon sink to global warming. Between 2000 and 2019, warming weakened the oceanic uptake of CO_2 (ref. 39), but the impact was much weaker than expected

from decreased solubility alone (that is, the thermal driver). This is because the temperature-induced outgassing of CO_2 and the reduced upwelling of DIC (both non-thermal drivers) caused a negative feedback that compensated the initial perturbation. While these negative feedbacks have been demonstrated for historic warming SST extremes^{22–24} and historic trends in the ocean carbon sink, it remains unclear whether these stabilizing mechanisms of the ocean carbon sink will remain effective under future extreme SST events, which are expected to become more frequent, intense and longer lasting⁵, or progressing global warming. Deviations from the negative feedbacks observed in the past could, for example, occur if longer-lasting SST extremes cause stronger limitations of CO_2 outgassing due to DIC depletion or if the efficiency of the biological carbon pump becomes more strongly affected. To keep track of changes in the ocean carbon sink, the continued, revived and extended observation of the ocean through high-quality $f\text{CO}_2$ measurements remains indispensable and it needs to be accompanied by an improved understanding of the $f\text{CO}_2$ mapping skill at seasonal to interannual timescales and across ocean biomes^{40,41}.

Online content

Any methods, additional references, Nature Portfolio reporting summaries, source data, extended data, supplementary information, acknowledgements, peer review information; details of author contributions and competing interests; and statements of data and code availability are available at <https://doi.org/10.1038/s41558-025-02380-4>.

References

1. Friedlingstein, P. et al. Global carbon budget 2023. *Earth Syst. Sci. Data* **15**, 5301–5369 (2023).
2. Gruber, N. et al. Trends and variability in the ocean carbon sink. *Nat. Rev. Earth Environ.* <https://doi.org/10.1038/s43017-022-00381-x> (2023).
3. Müller, J. D. et al. Decadal trends in the oceanic storage of anthropogenic carbon from 1994 to 2014. *AGU Adv.* **4**, e2023AV000875 (2023).
4. IPCC *Climate Change 2021: The Physical Science Basis* (eds Masson-Delmotte, V. et al.) (Cambridge Univ. Press, 2021).
5. Frölicher, T. L., Fischer, E. M. & Gruber, N. Marine heatwaves under global warming. *Nature* **560**, 360–364 (2018).

6. Jo, A. R., Lee, J.-Y., Sharma, S. & Lee, S.-S. Season-dependent atmosphere-ocean coupled processes driving SST seasonality changes in a warmer climate. *Geophys. Res. Lett.* **51**, e2023GL106953 (2024).
7. Shi, J.-R., Santer, B. D., Kwon, Y.-O. & Wijffels, S. E. The emerging human influence on the seasonal cycle of sea surface temperature. *Nat. Clim. Change* <https://doi.org/10.1038/s41558-024-01958-8> (2024).
8. Huang, B. et al. Record high sea surface temperatures in 2023. *Geophys. Res. Lett.* **51**, e2024GL108369 (2024).
9. Samset, B. H., Lund, M. T., Fuglestvedt, J. S. & Wilcox, L. J. 2023 temperatures reflect steady global warming and internal sea surface temperature variability. *Commun. Earth Environ.* **5**, 460 (2024).
10. Raghuraman, S. P. et al. The 2023 global warming spike was driven by the El Niño–Southern Oscillation. *Atmos. Chem. Phys.* **24**, 11275–11283 (2024).
11. Terhaar, J., Burger, F. A., Vogt, L., Frölicher, T. L. & Stocker, T. F. Record sea surface temperature jump in 2023–2024 unlikely but not unexpected. *Nature* **639**, 942–946 (2025).
12. Jiang, N. et al. El Niño and sea surface temperature pattern effects lead to historically high global mean surface temperatures in 2023. *Geophys. Res. Lett.* **52**, e2024GL113733 (2025).
13. Kuhlbrodt, T., Swaminathan, R., Ceppi, P. & Wilder, T. A glimpse into the future: the 2023 ocean temperature and sea ice extremes in the context of longer-term climate change. *Bull. Am. Meteorol. Soc.* **105**, E474–E485 (2024).
14. England, M. H. et al. Drivers of the extreme North Atlantic marine heatwave during 2023. *Nature* **642**, 636–643 (2025).
15. Weiss, R. F. Carbon dioxide in water and seawater: the solubility of a non-ideal gas. *Mar. Chem.* **2**, 203–215 (1974).
16. Takahashi, T., Olafsson, J., Goddard, J. G., Chipman, D. W. & Sutherland, S. C. Seasonal variation of CO₂ and nutrients in the high-latitude surface oceans: a comparative study. *Glob. Biogeochem. Cycles* **7**, 843–878 (1993).
17. McKinley, G. A., Fay, A. R., Eddebar, Y. A., Gloege, L. & Lovenduski, N. S. External forcing explains recent decadal variability of the ocean carbon sink. *AGU Adv.* **1**, e2019AV000149 (2020).
18. Sarmiento, J. L. & Gruber, N. *Ocean Biogeochemical Dynamics* (Princeton Univ. Press, 2006).
19. Landschützer, P., Gruber, N., Bakker, D. C. E., Stemmler, I. & Six, K. D. Strengthening seasonal marine CO₂ variations due to increasing atmospheric CO₂. *Nat. Clim. Change* **8**, 146–150 (2018).
20. Rodgers, K. B. et al. Seasonal variability of the surface ocean carbon cycle: a synthesis. *Glob. Biogeochem. Cycles* **37**, e2023GB007798 (2023).
21. Liao, E., Resplandy, L., Liu, J. & Bowman, K. W. Amplification of the ocean carbon sink during El Niños: role of poleward Ekman transport and influence on atmospheric CO₂. *Glob. Biogeochem. Cycles* **34**, e2020GB006574 (2020).
22. Mignot, A. et al. Decrease in air-sea CO₂ fluxes caused by persistent marine heatwaves. *Nat. Commun.* **13**, 4300 (2022).
23. Burger, F. A., Terhaar, J. & Frölicher, T. L. Compound marine heatwaves and ocean acidity extremes. *Nat. Commun.* **13**, 4722 (2022).
24. Li, C., Burger, F. A., Raible, C. C. & Frölicher, T. L. Observed regional impacts of marine heatwaves on sea-air CO₂ Exchange. *Geophys. Res. Lett.* **51**, e2024GL110379 (2024).
25. Bennington, V., Galjanic, T. & McKinley, G. A. Explicit physical knowledge in machine learning for ocean carbon flux reconstruction: the pCO₂-residual method. *J. Adv. Model. Earth Syst.* **14**, e2021MS002960 (2022).
26. Chau, T.-T.-T., Chevallier, F. & Gehlen, M. Global analysis of surface ocean CO₂ fugacity and air-sea fluxes with low latency. *Geophys. Res. Lett.* **51**, e2023GL106670 (2024).
27. Landschützer, P., Gruber, N. & Bakker, D. C. E. Decadal variations and trends of the global ocean carbon sink. *Glob. Biogeochem. Cycles* **30**, 1396–1417 (2016).
28. Gregor, L., Shutler, J. & Gruber, N. High-resolution variability of the ocean carbon sink. *Glob. Biogeochem. Cycles* **38**, e2024GB008127 (2024).
29. Hauck, J., Mayot, N., Landschützer, P. & Jersild, A. Global Carbon Budget 2024, surface ocean fugacity of CO₂ (fCO₂) and air-sea CO₂ flux of individual global ocean biogeochemical models and surface ocean fCO₂-based data-products. *Zenodo* <https://doi.org/10.5281/zenodo.14092496> (2025).
30. Bakker, D. C. E. et al. A multi-decade record of high-quality fCO₂ data in version 3 of the Surface Ocean CO₂ Atlas (SOCAT). *Earth Syst. Sci. Data* **8**, 383–413 (2016).
31. González-Dávila, M., Santana Casiano, J. M. & Machín, F. Changes in the partial pressure of carbon dioxide in the Mauritanian–Cap Vert upwelling region between 2005 and 2012. *Biogeosciences* **14**, 3859–3871 (2017).
32. Bates, N. R., Takahashi, T., Chipman, D. W. & Knap, A. H. Variability of pCO₂ on diel to seasonal timescales in the Sargasso Sea near Bermuda. *J. Geophys. Res. Oceans* **103**, 15567–15585 (1998).
33. Sutton, A. J. et al. A high-frequency atmospheric and seawater pCO₂ data set from 14 open-ocean sites using a moored autonomous system. *Earth Syst. Sci. Data* **6**, 353–366 (2014).
34. Gürses, Ö. et al. Ocean biogeochemistry in the coupled ocean–sea ice–biogeochemistry model FESOM2.1–RECoM3. *Geosci. Model Dev.* **16**, 4883–4936 (2023).
35. Yang, S. & Gruber, N. The anthropogenic perturbation of the marine nitrogen cycle by atmospheric deposition: nitrogen cycle feedbacks and the ¹⁵N Haber–Bosch effect. *Glob. Biogeochem. Cycles* **30**, 1418–1440 (2016).
36. Tsujino, H. et al. JRA-55 based surface dataset for driving ocean–sea–ice models (JRA55-do). *Ocean Model.* **130**, 79–139 (2018).
37. Chatterjee, A. et al. Influence of El Niño on atmospheric CO₂ over the tropical Pacific Ocean: findings from NASA’s OCO-2 mission. *Science* **358**, eaam5776 (2017).
38. Feely, R. A., Wanninkhof, R., Takahashi, T. & Tans, P. Influence of El Niño on the equatorial Pacific contribution to atmospheric CO₂ accumulation. *Nature* **398**, 597–601 (1999).
39. Bunsen, F., Nissen, C. & Hauck, J. The impact of recent climate change on the global ocean carbon sink. *Geophys. Res. Lett.* **51**, e2023GL107030 (2024).
40. Gloege, L. et al. Quantifying errors in observationally based estimates of ocean carbon sink variability. *Glob. Biogeochem. Cycles* **35**, e2020GB006788 (2021).
41. Hauck, J. et al. Sparse observations induce large biases in estimates of the global ocean CO₂ sink: an ocean model subsampling experiment. *Philos. Trans. R. Soc. A* **381**, 20220063 (2023).

Publisher's note Springer Nature remains neutral with regard to jurisdictional claims in published maps and institutional affiliations.

Open Access This article is licensed under a Creative Commons Attribution 4.0 International License, which permits use, sharing, adaptation, distribution and reproduction in any medium or format, as long as you give appropriate credit to the original author(s) and the source, provide a link to the Creative Commons licence, and indicate if changes were made. The images or other third party material in this article are included in the article's Creative Commons licence, unless indicated otherwise in a credit line to the material. If material is not included in the article's Creative Commons licence and your intended use is not permitted by statutory regulation or exceeds the permitted use, you will need to obtain permission directly from the copyright holder. To view a copy of this licence, visit <http://creativecommons.org/licenses/by/4.0/>.

Methods

Data sources

This study relied on four $f\text{CO}_2$ products and two global ocean biogeochemical models, for which technical details are provided in Extended Data Tables 1 and 2, respectively. These data sources constitute a subset of those used in the Global Carbon Budget^{1,29} (except for the $f\text{CO}_2$ -Residual product) and the second iteration of the Regional Carbon Cycle Assessment and Processes project (RECCAP2)^{42,43}. The observation-based SST fields used as predictor variables in the $f\text{CO}_2$ products were also used for our analysis of SST trends and anomalies. The GOBM simulations used in this study are equivalent to those considered as ‘simulation A’ in RECCAP2, that is, they are forced with (1) reanalysis data to represent the observed climate variability over the hindcast period and (2) historic atmospheric CO_2 observations to represent anthropogenic emissions.

Biome definition

To average or integrate surface ocean properties regionally, we used ocean biomes originally defined by Fay and McKinley⁴⁴ and slightly modified for use in the RECCAP2 project^{43,45–47}. We used a single, time-invariant definition of the biome boundaries (Extended Data Fig. 2a) to obtain estimates that are directly comparable across data products, across seasons and to numerous previous studies.

Anomaly determination against moving baseline

All anomalies determined in this study are expressed relative to a moving baseline to remove long-term trends driven by the growth in atmospheric CO_2 or global warming. The moving baseline for any variable of interest was determined by fitting a linear regression model to the historic observations from 1990 through 2022 as a function of the calendar year. The baseline estimate for a given year, including 2023, was then obtained as the predicted value of this linear regression model. The underlying data are either annual or monthly mean values. The data for 2023 were excluded from the regression to achieve a baseline estimate that is unbiased from the actual anomaly in 2023. For the atmospheric and surface ocean $f\text{CO}_2$, the linear regression model was replaced by a quadratic fit to better approximate the actual evolution of their growth rates over time. Finally, anomalies were calculated by subtracting the predicted baseline value from the observed value.

Expected $f\text{CO}_2$ anomaly in 2023

To determine the expected $f\text{CO}_2$ anomaly in 2023 for the global non-polar ocean, we fitted linear regression models of the integrated annual mean $f\text{CO}_2$ anomaly as a function of the annual mean SST anomaly to the hindcast estimates of our four $f\text{CO}_2$ products from 1990 through 2022. The intercepts (in PgC yr^{-1}) and slopes (in $\text{PgC yr}^{-1} \text{ }^\circ\text{C}^{-1}$) of these four regression models were determined to be $-7.3 \times 10^{-15} \text{ PgC yr}^{-1}$ and $-0.55 \text{ PgC yr}^{-1} \text{ }^\circ\text{C}^{-1}$ (CMEMS), $2.1 \times 10^{-15} \text{ PgC yr}^{-1}$ and $-0.79 \text{ PgC yr}^{-1} \text{ }^\circ\text{C}^{-1}$ ($f\text{CO}_2$ -Residual), $-5.7 \times 10^{-15} \text{ PgC yr}^{-1}$ and $-0.40 \text{ PgC yr}^{-1} \text{ }^\circ\text{C}^{-1}$ (OceanSODAv2), and $-3.4 \times 10^{-15} \text{ PgC yr}^{-1}$ and $-0.30 \text{ PgC yr}^{-1} \text{ }^\circ\text{C}^{-1}$ (SOM-FFN), respectively.

Based on these regression models, the expected $f\text{CO}_2$ anomaly in 2023 was calculated for each $f\text{CO}_2$ product from the SST anomaly in 2023. The 2023 SST anomalies (in $\text{ }^\circ\text{C}$) and the derived expected $f\text{CO}_2$ anomalies (in PgC yr^{-1}) are $0.19 \text{ }^\circ\text{C}$ and $-0.10 \text{ PgC yr}^{-1}$ (CMEMS), $0.2 \text{ }^\circ\text{C}$ and $-0.16 \text{ PgC yr}^{-1}$ ($f\text{CO}_2$ -Residual), $0.22 \text{ }^\circ\text{C}$ and $-0.09 \text{ PgC yr}^{-1}$ (OceanSODAv2), and $0.23 \text{ }^\circ\text{C}$ and $-0.07 \text{ PgC yr}^{-1}$ (SOM-FFN), respectively. The mean and standard deviation of this expected $f\text{CO}_2$ anomaly are $-0.11 \pm 0.04 \text{ PgC yr}^{-1}$ (Fig. 1b).

In addition to the approach outlined above, we investigated two alternative methods to constrain the expected flux anomaly. First, we used the actual spatial distribution of the SST anomalies in 2023 (Fig. 1c) and multiplied those by the slope of a linear regression between air-sea CO_2 flux anomalies and SST anomalies from 1990 through 2022 to obtain a spatially resolved map of expected flux anomalies in

2023 (Extended Data Fig. 1a,b). The globally integrated expected flux anomaly for 2023 from this approach ($-0.10 \pm 0.02 \text{ PgC yr}^{-1}$) is almost identical to that obtained from our standard approach, that is, the regression of global annual mean SST and integrated flux anomalies ($-0.11 \pm 0.04 \text{ PgC yr}^{-1}$). Second, we fitted a multiple linear regression model that considers the concentration and growth rate of atmospheric CO_2 , as well as SST anomalies in the equatorial Pacific as an indicator of the El Niño and Southern Oscillation (ENSO) state, as predictor variables for the annual mean ocean carbon sink from 1990 through 2022. This model was used to predict the expected carbon sink over time, providing an expected value of $-0.21 \pm 0.07 \text{ PgC yr}^{-1}$ for 2023. The unexpected component of the global non-polar ocean carbon sink, which is the difference between the expected and the observed value, is very similar when using this multiple linear regression model or the linear baseline approach together with the expected CO_2 flux anomaly based on the global mean SST anomaly (Extended Data Fig. 1c). As for our standard approach, these alternative methods were applied to each $f\text{CO}_2$ product individually and the results are reported as the mean and standard deviation across products.

Computation and attribution of flux anomalies

The $f\text{CO}_2$ flux ($f\text{CO}_2$) across the air-sea interface is calculated as the product of the fugacity difference between ocean and atmosphere ($\Delta f\text{CO}_2$), the gas transfer velocity (k_w) and the solubility of CO_2 in seawater (K_0) and is scaled with the fractional ice coverage (f_{ice}) according to:

$$f\text{CO}_2 = \Delta f\text{CO}_2 \times (k_w K_0) \times (1 - f_{\text{ice}}) \quad (1)$$

To attribute flux anomalies to the underlying anomalies in the drivers, we applied a classical Reynolds decomposition. For this purpose, we considered the product $k_w K_0$ as a single term that is largely temperature independent because the temperature dependence in k_w and K_0 tend to cancel out. While the exact degree of this cancellation depends on the chosen parameterization of k_w and K_0 , widely used formulations^{15,48} suggest a gradual increase in k_w of 120% and a decrease in K_0 of 50% on a temperature increase from 0 to $30 \text{ }^\circ\text{C}$. In contrast, the corresponding $k_w K_0$ changes by less than 10% over the same temperature range. As a consequence, $k_w K_0$ depends primarily on the prevailing wind speed. Furthermore, we neglected the modulation of $f\text{CO}_2$ by the fractional ice coverage as this study focused on ice-free ocean. To derive the Reynolds decomposition, in general, the individual components in equation (1) can be described as:

$$f\text{CO}_2 = f\text{CO}_{2,\text{baseline}} + 'f\text{CO}_2 \quad (2)$$

$$\Delta f\text{CO}_2 = \Delta f\text{CO}_{2,\text{baseline}} + '\Delta f\text{CO}_2 \quad (3)$$

$$(k_w K_0) = (k_w K_0)_{\text{baseline}} + '(k_w K_0) \quad (4)$$

where prime symbols ('') and ‘baseline’ denote anomalies and detrended baseline estimates, respectively.

Inserting equations (3) and (4) into equation (1) and expanding the product leads to:

$$f\text{CO}_2 = \Delta f\text{CO}_{2,\text{baseline}} \times (k_w K_0)_{\text{baseline}} + '\Delta f\text{CO}_2 \times (k_w K_0)_{\text{baseline}} + \Delta f\text{CO}_{2,\text{baseline}} \times '(k_w K_0) + '\Delta f\text{CO}_2 \times '(k_w K_0) \quad (5)$$

The first term in equation (5), that is, the product $\Delta f\text{CO}_{2,\text{baseline}} \times (k_w K_0)_{\text{baseline}}$, represents the baseline flux $f\text{CO}_{2,\text{baseline}}$ in equation (2), whereas the three other terms describe the flux anomaly ‘ $f\text{CO}_2$ ’. Hence, we can decompose the observed flux anomaly into its components according to:

$$'f\text{CO}_2 = '\Delta f\text{CO}_2 \times (k_w K_0)_{\text{baseline}} + \Delta f\text{CO}_{2,\text{baseline}} \times '(k_w K_0) + '\Delta f\text{CO}_2 \times '(k_w K_0) \quad (6)$$

We initially computed the flux anomaly contributions according to equation (6) using the original grid of our estimates (monthly, $1^\circ \times 1^\circ$) and then averaged the components in space and time (for example, to compute biome annual means).

Thermal and non-thermal decomposition of $f\text{CO}_2$ anomalies

To assess the mechanistic drivers causing the 2023 anomalies in $\Delta f\text{CO}_2$, we decomposed the main contributor to this anomaly, that is, the surface ocean $f\text{CO}_2$ anomaly, into a thermal and non-thermal component based on the SST anomalies. We performed this decomposition initially on the original grid of our estimates (monthly, $1^\circ \times 1^\circ$) and then averaged the components in space and time (for example, to compute biome annual means).

Specifically, we determined in a first step the thermally driven $f\text{CO}_2$ anomaly ($'f\text{CO}_{2,\text{thermal}}$) according to equation (7):

$$'f\text{CO}_{2,\text{thermal}} = f\text{CO}_{2,\text{baseline}} \times \exp(\gamma_T \times \text{'SST}) - f\text{CO}_{2,\text{baseline}} \quad (7)$$

where $f\text{CO}_{2,\text{baseline}}$ is the monthly baseline value of $f\text{CO}_2$, γ_T is the temperature sensitivity of $f\text{CO}_2$ (0.0423 K^{-1} ¹⁶) and 'SST' is the monthly anomaly in SST determined against a linear regression baseline fitted to the monthly SST data from 1990 through 2022. Note that $f\text{CO}_{2,\text{baseline}}$ inherits a seasonal cycle and is expressed in absolute values that are similar to the observed $f\text{CO}_2$ values. In contrast, 'SST' represents only the deviation of the observed SST from the expected baseline value, that is, it is a numerically small value of positive or negative sign and does not follow a classical seasonal cycle. As a consequence, the variable $'f\text{CO}_{2,\text{thermal}}$ computed according to equation (7) is also a numerically small value of positive or negative sign and does not follow a typical seasonal pattern. In this regard, our thermal anomaly component $'f\text{CO}_{2,\text{thermal}}$ differs from the widely used thermal component of $f\text{CO}_2$ that is defined as $f\text{CO}_{2,\text{thermal}} = f\text{CO}_{2,\text{mean}} \times \exp[\gamma_T \times (\text{SST}_{\text{obs}} - \text{SST}_{\text{mean}})]$, where $f\text{CO}_{2,\text{mean}}$ and SST_{mean} are the regional annual mean values of the surface ocean CO_2 fugacity and SST, respectively, and SST_{obs} is the actual observed monthly SST. In this classical decomposition of absolute $f\text{CO}_2$ values (instead of anomalies), $\text{SST}_{\text{obs}} - \text{SST}_{\text{mean}}$ and hence also $'f\text{CO}_{2,\text{thermal}}$ follow a classical seasonal cycle and the value of $'f\text{CO}_{2,\text{thermal}}$ has the same order of magnitude as $f\text{CO}_2$ itself. $f\text{CO}_{2,\text{thermal}}$ can be considered as the seasonal cycle of $f\text{CO}_2$ driven solely by the seasonal cycle in SST.

Based on $'f\text{CO}_{2,\text{thermal}}$ and the directly determined total $f\text{CO}_2$ anomaly ($'f\text{CO}_2$), we calculated the non-thermally driven $f\text{CO}_2$ anomaly ($'f\text{CO}_{2,\text{non-thermal}}$) according to:

$$'f\text{CO}_{2,\text{non-thermal}} = 'f\text{CO}_2 - 'f\text{CO}_{2,\text{thermal}} \quad (8)$$

While our definition of $'f\text{CO}_{2,\text{non-thermal}}$ according to equation (8) resembles the definition of the $f\text{CO}_2$ residual in previous studies^{25,28}, it differs in that it does not inherit a classical seasonal cycle. Similarly, our anomaly component $'f\text{CO}_{2,\text{non-thermal}}$ differs from the widely used^{19,49} non-thermal component of $f\text{CO}_2$ that is defined as $f\text{CO}_{2,\text{non-thermal}} = f\text{CO}_{2,\text{obs}} \times \exp[\gamma_T \times (\text{SST}_{\text{mean}} - \text{SST}_{\text{obs}})]$, with $f\text{CO}_{2,\text{obs}}$ being the observed monthly surface ocean CO_2 fugacity, and describes the $f\text{CO}_2$ seasonality that would occur if the SST remained at the annual mean, but all other processes followed their natural seasonal cycle.

Conversion from DIC to $f\text{CO}_2$ anomalies

To convert DIC anomalies into $f\text{CO}_2$ anomalies, it is important to consider TA anomalies that occur simultaneously because the fraction of the DIC anomaly that is caused by the TA anomaly has no effect on $f\text{CO}_2$. The conversion can formally be derived by considering the sensitivity of $f\text{CO}_2$ to changes in either DIC (γ_{DIC}) or TA (γ_{TA}) (ref. 50):

$$\gamma_{\text{DIC}} = (\Delta f\text{CO}_{2,\text{DIC}}/f\text{CO}_2)/\Delta \text{DIC} \quad (9)$$

and

$$\gamma_{\text{TA}} = (\Delta f\text{CO}_{2,\text{TA}}/f\text{CO}_2)/\Delta \text{TA}, \quad (10)$$

where ΔDIC and ΔTA denote changes in DIC and TA, respectively, $\Delta f\text{CO}_{2,\text{DIC}}$ and $\Delta f\text{CO}_{2,\text{TA}}$ denote changes in $f\text{CO}_2$ exclusively due to ΔDIC and ΔTA , respectively, and $f\text{CO}_2$ denotes the surface ocean CO_2 fugacity in absolute terms. Given that the total change in $f\text{CO}_2$ is the sum of the change driven by TA and DIC:

$$\Delta f\text{CO}_2 = \Delta f\text{CO}_{2,\text{DIC}} + \Delta f\text{CO}_{2,\text{TA}} \quad (11)$$

the two sensitivities γ_{DIC} and γ_{TA} can be inserted into equation (11) to derive the expression:

$$\Delta f\text{CO}_2 = \gamma_{\text{DIC}} \times f\text{CO}_2 \times \Delta \text{DIC} + \gamma_{\text{TA}} \times f\text{CO}_2 \times \Delta \text{TA} \quad (12)$$

We computed $\Delta f\text{CO}_2$ according to equation (12) using the output of our model simulations for $f\text{CO}_2$, ΔDIC and ΔTA and computing γ_{DIC} and γ_{TA} from the model temperature.

To support the mechanistic interpretation of equation (12), the approximation $\gamma_{\text{DIC}} \approx -\gamma_{\text{TA}}$ can be introduced. This approximation is valid, given that the global surface ocean γ_{DIC} and γ_{TA} are of very similar magnitude but opposite sign⁵⁰. Inserting the approximation into equation (12) leads to the expression:

$$\Delta f\text{CO}_2 = \gamma_{\text{DIC}} \times f\text{CO}_2 \times (\Delta \text{DIC} - \Delta \text{TA}) \quad (13)$$

The term $\Delta \text{DIC} - \Delta \text{TA}$ can be interpreted as the effective change in DIC that is not compensated for by a change in TA. Intuitively, a positive DIC anomaly that is not fully balanced by a TA anomaly would lead to a positive $f\text{CO}_2$ anomaly.

Interestingly, the approximation for carbonate ion concentration $[\text{CO}_3^{2-}] \approx \text{TA} - \text{DIC}$ can also be introduced¹⁸. Hence, the change in $f\text{CO}_2$ can also be expressed as:

$$\Delta f\text{CO}_2 = -\gamma_{\text{DIC}} (f\text{CO}_2/\text{DIC}) \Delta [\text{CO}_3^{2-}] \quad (14)$$

While equations (13) and (14) were not used to compute $\Delta f\text{CO}_2$, they are useful to illustrate that a negative anomaly in $f\text{CO}_2$ is in essence equivalent to a positive anomaly in carbonate ion concentration. Hence, Fig. 4c could be redrawn with an inverted colour scale and show $[\text{CO}_3^{2-}]$ instead of $\text{DIC} - \text{TA}$.

Data availability

The surface ocean $f\text{CO}_2$ observations that were used for the training and validation of the $f\text{CO}_2$ products are publicly available in SOCATv2023 (<https://doi.org/10.25921/r7xa-bt92>) and SOCATv2024 (<https://doi.org/10.25921/9wpn-th28>). For two stations, 2023 observations were sourced from SOCATv2024 and analysed in detail. Direct access to these data is possible via https://doi.org/10.3334/cdiac/otg.tsm_tao170w_On (TAO170W) and <https://doi.org/10.25921/r7vk-e838> (BATS). The $f\text{CO}_2$ products and GOBM simulations analysed in this study are available via Zenodo at <https://doi.org/10.5281/zenodo.14092496> (ref. 29).

Code availability

All code required to perform the analysis and prepare the figures presented in this study is available via Zenodo at <https://doi.org/10.5281/zenodo.15607822> (ref. 51).

References

- DeVries, T. et al. Magnitude, trends, and variability of the global ocean carbon sink from 1985 to 2018. *Glob. Biogeochem. Cycles* **37**, e2023GB007780 (2023).

43. Müller, J. D. RECCAP2-ocean data collection. Zenodo <https://doi.org/10.5281/zenodo.7990823> (2023).
44. Fay, A. R. & McKinley, G. A. Global open-ocean biomes: mean and temporal variability. *Earth Syst. Sci. Data* **6**, 273–284 (2014).
45. Pérez, F. F. et al. An assessment of CO₂ storage and sea-air fluxes for the Atlantic Ocean and Mediterranean Sea between 1985 and 2018. *Glob. Biogeochem. Cycles* **38**, e2023GB007862 (2024).
46. Hauck, J. et al. The Southern Ocean carbon cycle 1985–2018: mean, seasonal cycle, trends, and storage. *Glob. Biogeochem. Cycles* **37**, e2023GB007848 (2023).
47. Sarma, V. V. S. S. et al. Air-sea fluxes of CO₂ in the Indian Ocean between 1985 and 2018: a synthesis based on observation-based surface CO₂, hindcast and atmospheric inversion models. *Glob. Biogeochem. Cycles* **37**, e2023GB007694 (2023).
48. Wanninkhof, R. Relationship between wind speed and gas exchange over the ocean. *J. Geophys. Res. Oceans* **97**, 7373–7382 (1992).
49. Takahashi, T. et al. Global sea-air CO₂ flux based on climatological surface ocean pCO₂, and seasonal biological and temperature effects. *Deep Sea Res. Part II* **49**, 1601–1622 (2002).
50. Egleston, E. S., Sabine, C. L. & Morel, F. M. M. Revelle revisited: buffer factors that quantify the response of ocean chemistry to changes in DIC and alkalinity. *Glob. Biogeochem. Cycles* **24**, GB1002 (2010).
51. Müller, J. jens-daniel-mueller/heatwave_co2_flux_2023: acceptance NCC. Zenodo <https://doi.org/10.5281/zenodo.15607822> (2025).

Acknowledgements

We acknowledge the contributions from colleagues that helped us to realize this study and/or provided extensive comments, including, in alphabetical order, N. Bates, T.-T.-T. Chau, F. Chevallier, E. Claudel, A. Fay, M. González Dávila, Ö. Gürses, X. Lan, M. Larriere, D. Loher, J. M. Santana-Casiano, A. Sutton and J. Terhaar. J.D.M. and N.G. acknowledge support from the European Union's Horizon 2020 Research and Innovation programme under grant agreement nos. 821003 (project 4C) and 821001 (SO-CHIC). M.G. acknowledges funding support by the MOB TAC project of the European Copernicus Marine Environment Monitoring Service (CMEMS) and the European Union's Horizon Europe Research and Innovation programme under OceanICU (grant 101083922). Funding

to J.H. was provided by the Initiative and Networking Fund of the Helmholtz Association (Helmholtz Young Investigator Group MarESys, grant VH-NG-1301), the ERC-2022-STG OceanPeak (grant 101077209) and the European Union's Horizon Europe Research and Innovation programme under grant no. 101083922 (OceanICU). The work reflects only the authors' view; the European Commission and their executive agency are not responsible for any use that may be made. G.A.M. acknowledges support from NSF (LEAP STC AGS2019625, OCE2333608), NOAA (NA20OAR4310340) and ETH Zurich.

Author contributions

Conceptualization: J.D.M., N.G. and M.G. Methodology: J.D.M., A.S. and L.G. Software: J.D.M. and A.S. Validation: J.D.M. and A.S. Formal analysis: J.D.M. and A.S. Investigation: J.D.M. Resources: L.G., P.L., M.G., G.A.M., J.H., N.G. and D.C.E.B. Data curation: J.D.M. Writing—original draft: J.D.M. Writing—review and editing: all authors. Visualization: J.D.M.

Funding

Open access funding provided by Swiss Federal Institute of Technology Zurich.

Competing interests

The authors declare no competing interests.

Additional information

Extended data is available for this paper at <https://doi.org/10.1038/s41558-025-02380-4>.

Supplementary information The online version contains supplementary material available at <https://doi.org/10.1038/s41558-025-02380-4>.

Correspondence and requests for materials should be addressed to Jens Daniel Müller.

Peer review information *Nature Climate Change* thanks the anonymous reviewers for their contribution to the peer review of this work.

Reprints and permissions information is available at www.nature.com/reprints.

Extended Data Table 1 | Details of fCO₂ products

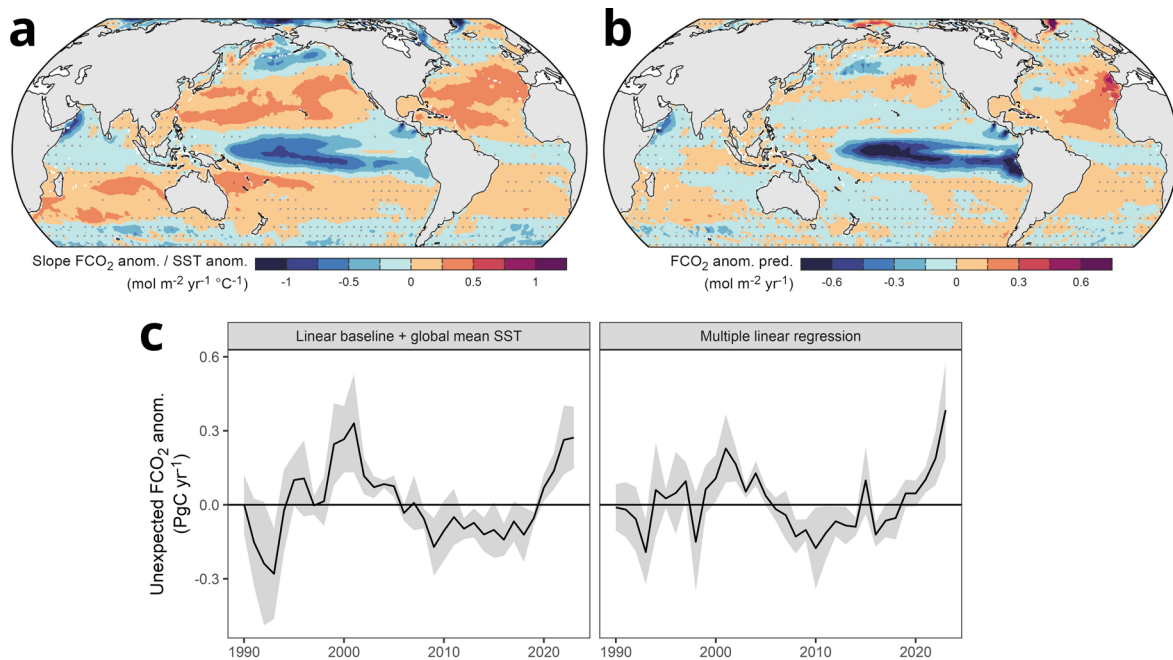
Product name	CMEMS	fCO ₂ -Residual	SOM-FFN	OceanSODAv2
Reference	Chau et al. (2022) (ref. 26)	Bennington et al. (2022) (ref. 25)	Landschützer et al. (2016) (ref. 27)	Gregor et al. (2024) (ref. 28)
Interpolation method	An ensemble of 100 feed-forward neural network models	EXtreme Gradient Boosting (XGB) algorithm applied to fCO ₂ -Residual (= pCO ₂ -pCO ₂ -T). For extension beyond training, xCO _{2,atm} trend is added to reconstructed fCO ₂ field.	Clustering-regression approach with self organising map (SOM) and feed-forward neural network (FFN)	Ensemble of clustering-regression approaches
Native resolution*	0.25°x0.25°; monthly	1°x1°; monthly	1°x1°; monthly	0.25°x0.25°; 8-daily
Sea surface fCO₂ training data	SOCATv2024; monthly, 1°x1°	SOCATv2024; monthly, 1°x1°	SOCATv2024; monthly, 1°x1°	SOCATv2024; monthly, 1°x1°
SST predictor	CMEMS	OISST	HadiSST	ESA
SSS predictor	CMEMS	EN4	EN4	SODA/ESA
SSH predictor	CMEMS	-	-	Ssalto/Duacs
Chl-a predictor	CMEMS	Globcolor merged CHL	Globcolor merged CHL	ESA
MLD predictor	ECCO2	deBoyer climatology	Merged MIMOC and deBoyer climatologies	SODA
K_w formulation	Wanninkhof (2014); a adjusted for global mean piston velocity = 16.5 cm/h; scaled by 1-f _{ice}	Wanninkhof (1992) with Schmidt number from Wanninkhof (2014); scaled to bomb 14C (Fay et al., 2021); scaled by 1-f _{ice}	Wanninkhof (1992); a adjusted for global mean piston velocity = 16cm/h; scaled by 1-f _{ice}	Wanninkhof (1992); scaled by 1-f _{ice}
Wind-speed	ERA5	CCMP2, ERA5, JRA55	ERA5	average of ERA5, JRA55, and NCEP1
Atmospheric CO₂	xCO ₂ from CAMS inversion; sea level pressure from ERA5; water vapor correction from Weiss (1980)	xCO ₂ from NOAA MBL; sea level pressure from ERA5; water vapor correction from Dickson (2007)	xCO ₂ from NOAA MBL; sea level pressure from NCEP; water vapor correction from Dickson (2007)	xCO ₂ from NOAA MBL; sea level pressure from ERA5; water vapor correction from Dickson (2007)
Sea-ice fraction (f_{ice})	OSTIA/CMEMS product	NOAA OISST	Rayner et al. (2003)	OSTIA

*All fCO₂ products and underlying predictor fields were regridded to a common spatial resolution of 1°x1° and monthly temporal resolution prior to the analysis presented in this study.

Extended Data Table. 2 | Details of GOBM simulations

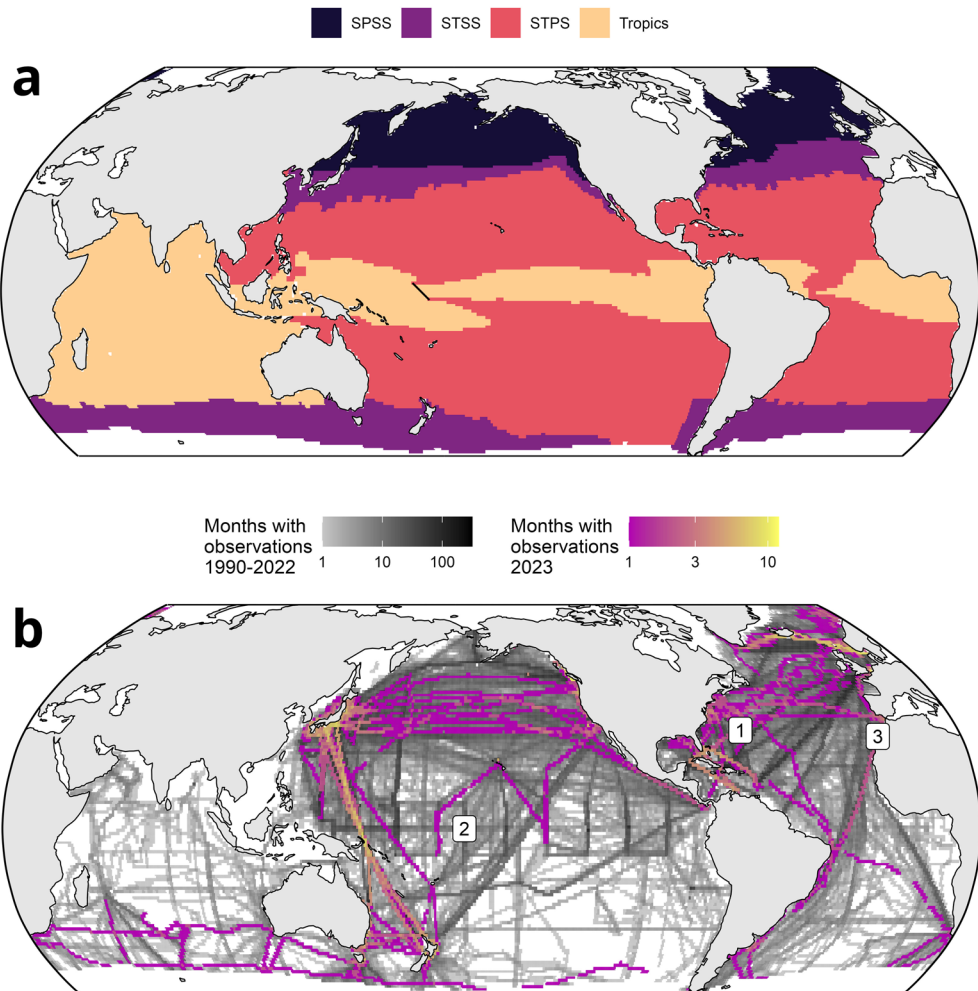
Model name	CESM-ETHZ	FESOM-RECoM
Reference	Doney et al. (2009); Lindsay et al. (2014); Yang and Gruber (2016) (ref. 35)	Gürses et al. (2023) (ref. 34)
Vertical layers	60	46
Native horizontal resolution	lon: 1.125° lat: 0.27° - 0.53°	1°; refined in equatorial, coastal, and polar regions
Initial conditions	POP2 model using Levitus data and a state of rest, carbonate chemistry from GLODAPv2 pre-industrial	DIC and TA (GLODAPv2 preindustrial); N, Si, and O ₂ (WOA13); Fe (PISCES, corrected with observations), temperature and salinity from PHC3.0 climatology
Spin up procedure	180 years with CORE forcing and 1850 pCO ₂ , switch to JRA forcing for 14 years; 3x cycling through JRA with historical forcing	Spun up from 1611-1957 with JRA55-do v1.3, repeating the year 1961.
Length of spin up	180 years (CORE) + 14 years (JRA)	1850-1957
Physical forcing	JRA-55 v1.3	JRA55-do v1.3
K_w parameters	a = 0.31 (Wanninkhof 1992), 1-fice	a = 0.251 (Wanninkhof 2014), 1-fice
Atmospheric CO₂	monthly, global mean xCO ₂ (Friedlingstein et al. 2022)	monthly, global mean xCO ₂ (Friedlingstein et al. 2022)

fice is the fractional ice coverage.



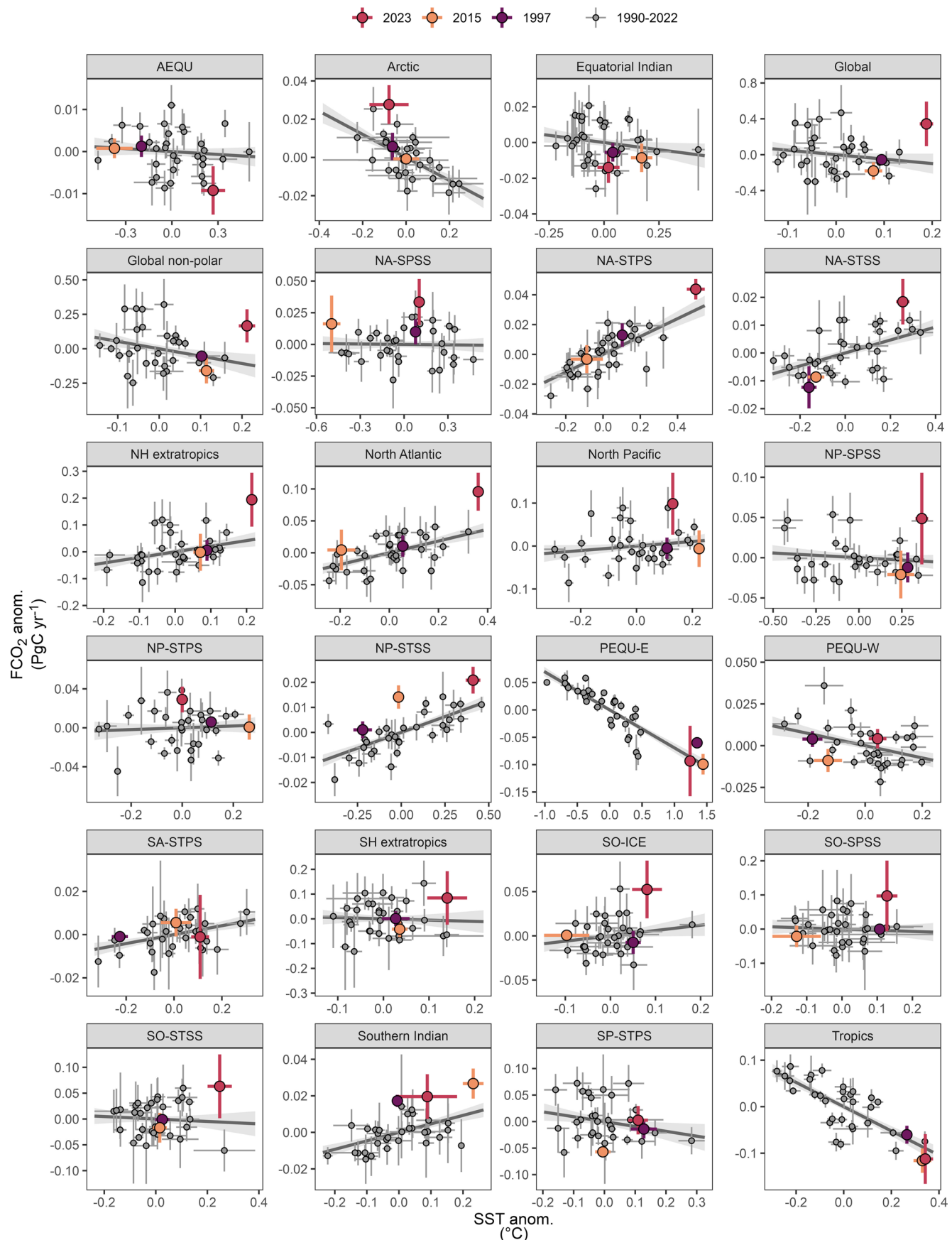
Extended Data Fig. 1 | Two alternative approaches to investigate the unexpected nature of the ocean carbon sink in 2023. (a) The slope of a linear regression between the air-sea CO_2 flux anomalies and SST anomalies in previous decades (1990–2022), which was multiplied with the actual spatial distribution in the SST anomalies in 2023 (Fig. 1a) to obtain (b) a predicted CO_2 flux anomaly map for 2023 that considers only the SST anomaly. (b) The unexpected part of the global non-polar ocean carbon sink, obtained from comparing the actual observed sink strength in each year to an expected value obtained from (left

panel) the linear regression baseline from Fig. 1b and the expected CO_2 flux anomaly based on the global mean SST anomaly and (right panel) a multiple linear regression model that was fitted with the atmospheric CO_2 , atmospheric CO_2 growth rate and SST in the equatorial Pacific as predictor variables and for the annual mean ocean carbon sink from 1990 through 2022 as target variable. The unexpected CO_2 flux anomalies in (c) represent the mean (black line) and standard deviation (grey ribbon) across our ensemble of four $f\text{CO}_2$ products.



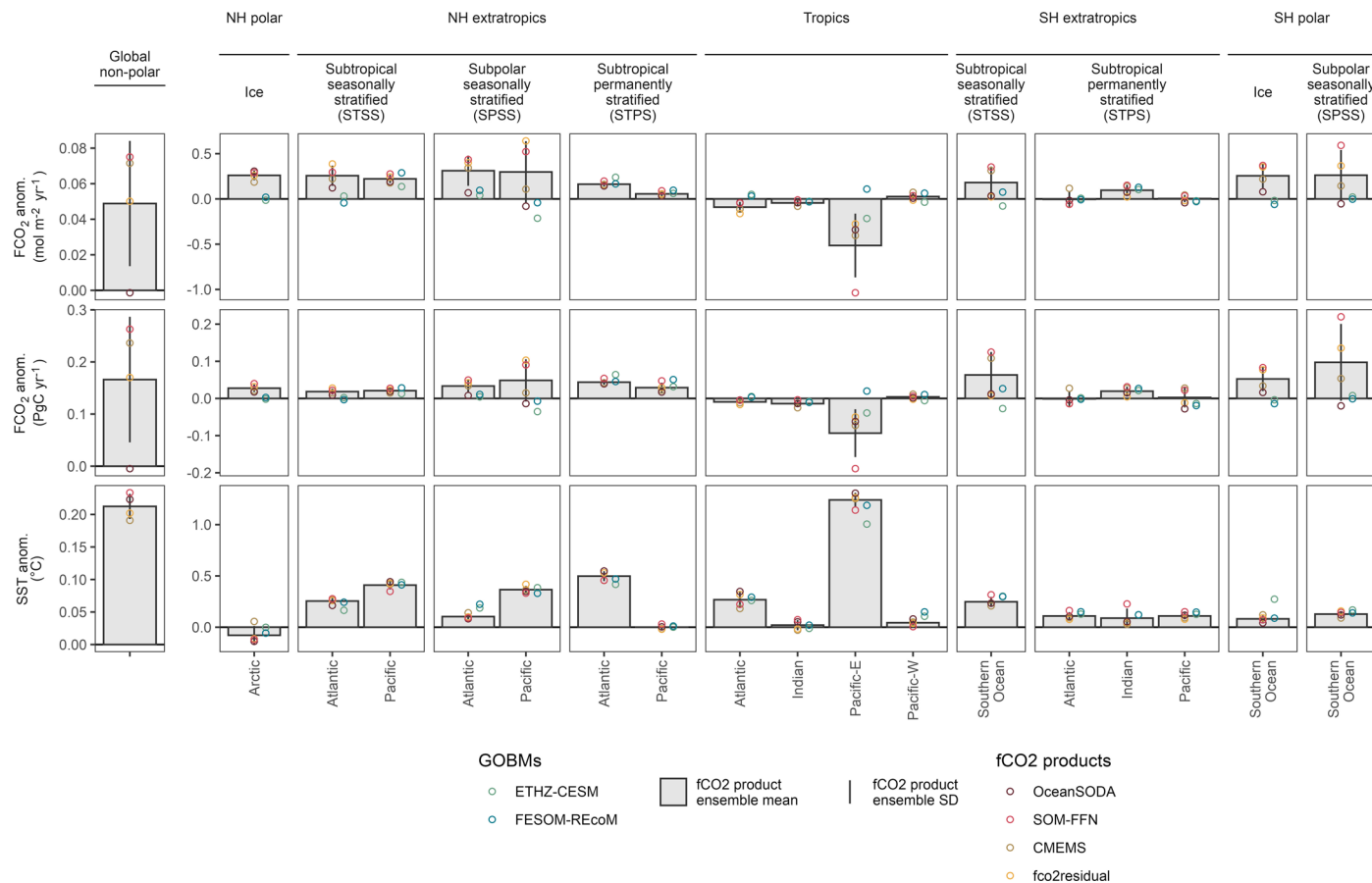
Extended Data Fig. 2 | Maps of ocean biomes and $f\text{CO}_2$ observations.
The abbreviations for the biome maps in (a) stand for the subpolar seasonally stratified (SPSS), subtropical seasonally stratified (STSS), subtropical permanently stratified (STPS) biomes. Note that the equatorial Pacific biome is split into an eastern and western part at the black line. These biomes are

used to regionally integrate or average spatially resolved estimates. The $f\text{CO}_2$ observations in (b) are available from SOCATv2024 for the historical period and 2023. The labels in panel (b) show the three stations for which 2023 observations are compared to the NRT $f\text{CO}_2$ product estimates (see SI): 1 = Bermuda Atlantic Time Series; 2 = Equatorial Pacific; 3 = VOS Line (Gran Canaria - Barcelona).

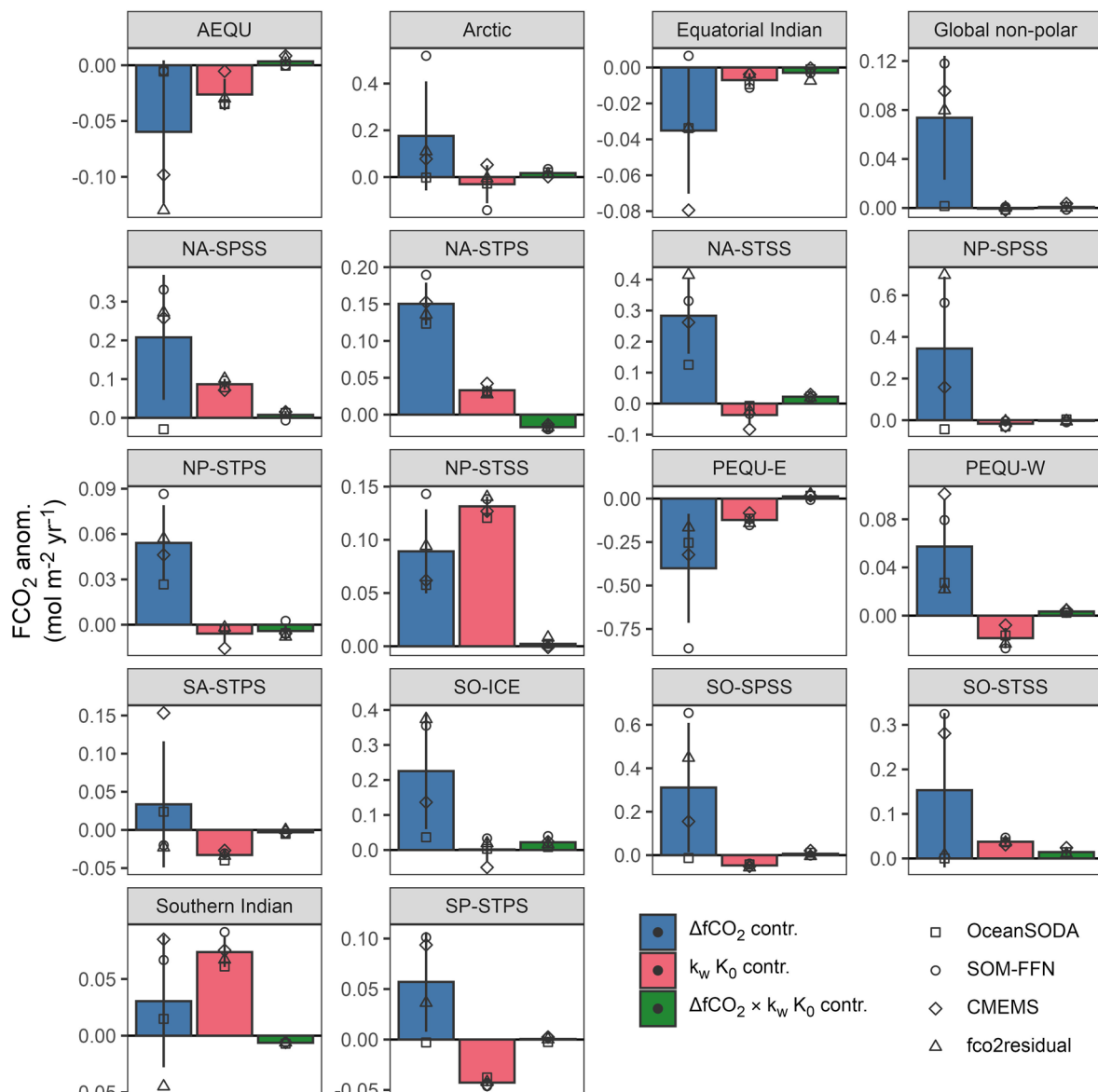


Extended Data Fig. 3 | Relationship between annual mean SST and $f\text{CO}_2$ anomalies from 1990 to 2023 for all biomes. Same as Fig. 2, but showing additional estimates for various biomes and regions as provided also in Table 1. Symbols and error bars represent the mean and standard deviation across the

ensemble of four observation-based $f\text{CO}_2$ products. The grey lines and ribbons indicate linear regressions and 68% confidence intervals across all annual mean anomalies from 1990 to 2022.

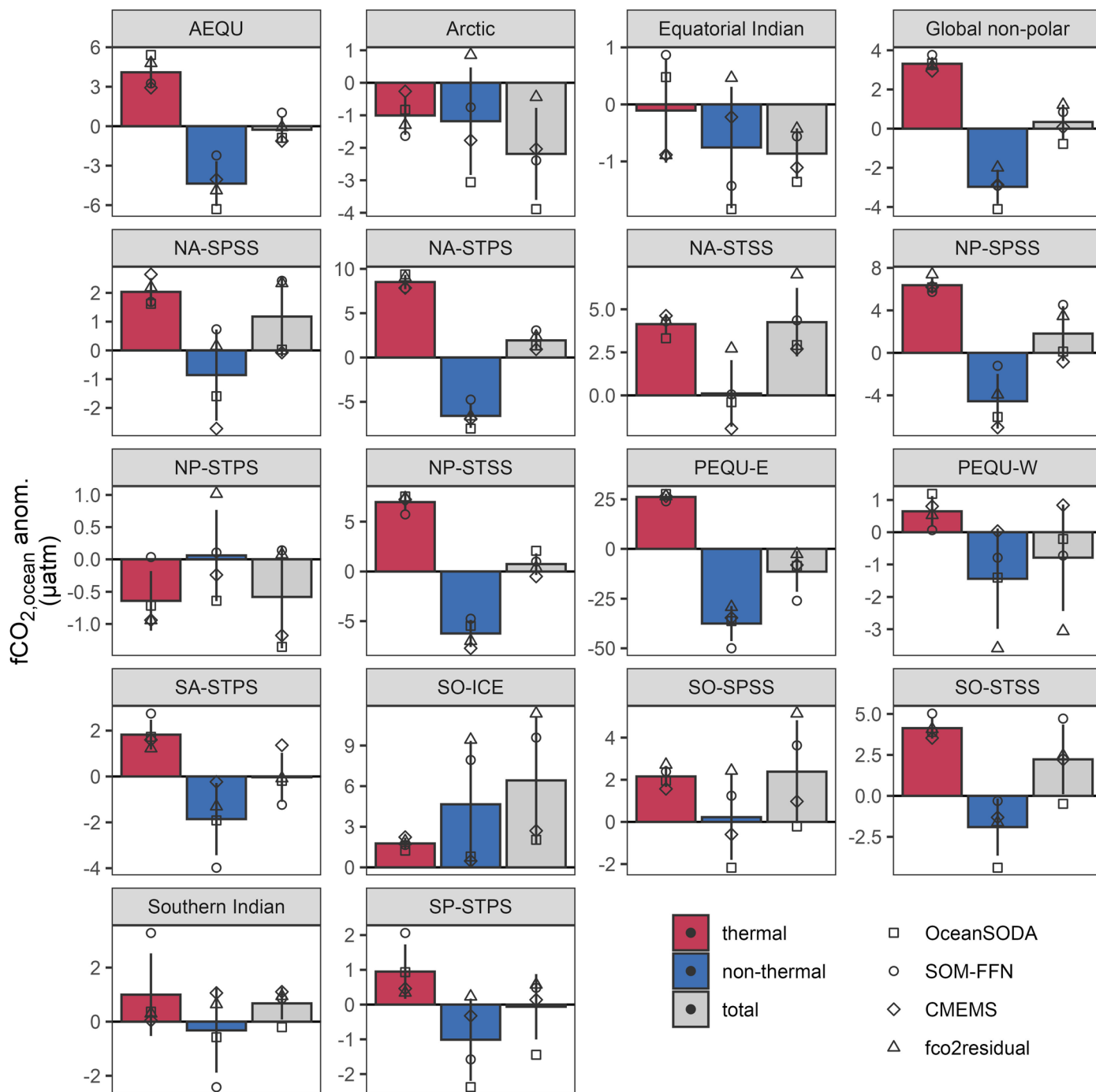


Extended Data Fig. 4 | Annual mean $f\text{CO}_2$ and SST anomalies in 2023 relative to a linear trend baseline. Anomaly estimates from Table 1 are displayed as bars ($f\text{CO}_2$ product ensemble mean) with uncertainty ranges (standard deviation across four $f\text{CO}_2$ products). In addition to the results in Table 1, estimates for the individual $f\text{CO}_2$ products and GOBMs are displayed as symbols.



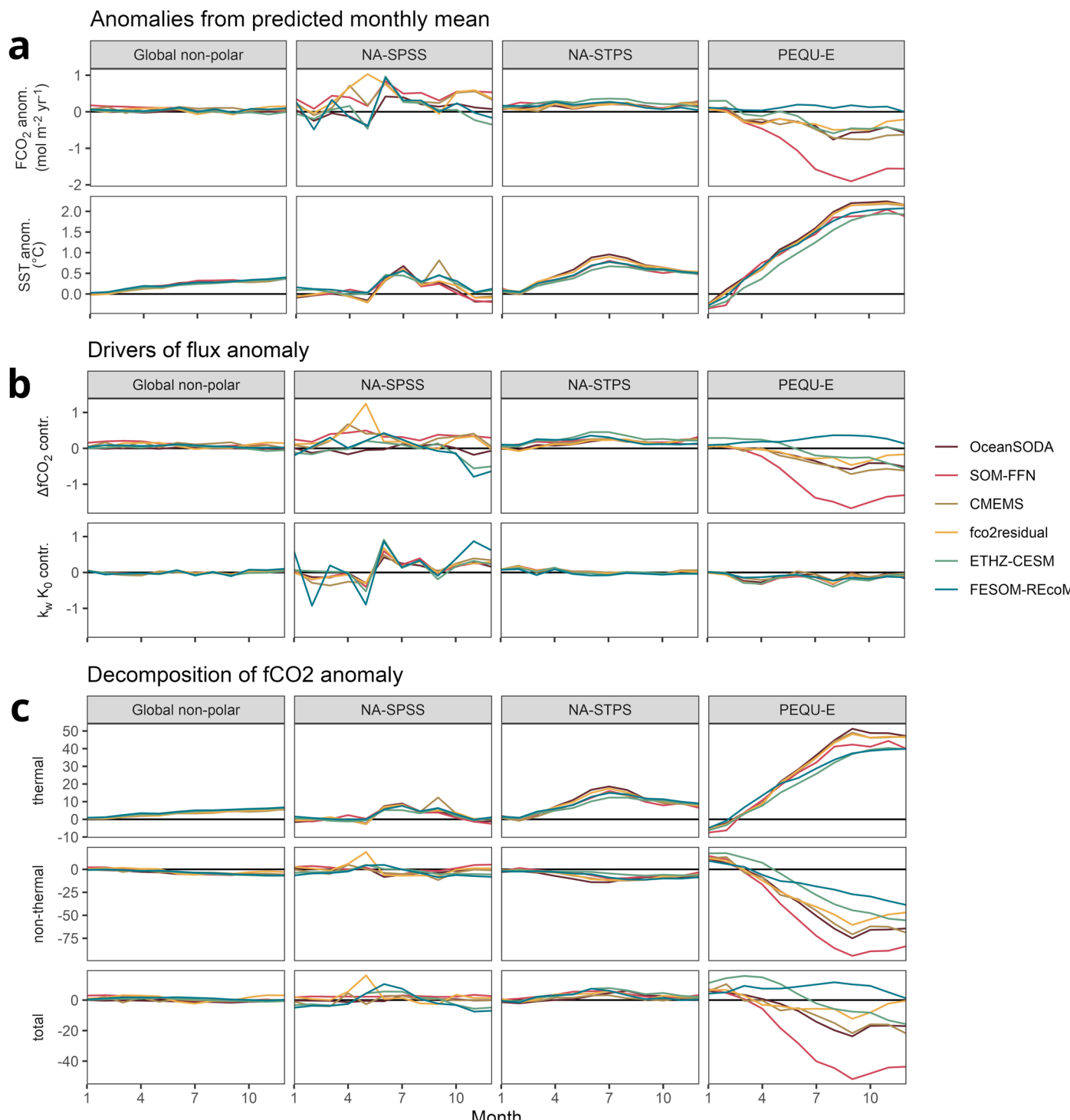
Extended Data Fig. 5 | Driver attribution of 2023 biome-mean annual mean CO₂ flux anomalies. Same estimates as shown in Fig. 3a-c, but averaging the attribution of the 2023 annual mean flux anomalies over the ocean biomes shown in Extended Data Fig. 2. Flux anomalies are attributed to their primary drivers, that is, the CO₂ fugacity gradient between ocean and atmosphere ($\Delta f\text{CO}_2$),

the product of the gas transfer velocity and the solubility of CO₂ ($k_w K_0$), which is primarily controlled by wind speed, as well as the cross product of both drivers ($\Delta f\text{CO}_2 \times k_w K_0$). Colored bars represent the mean, and uncertainty bars the standard deviation across the ensemble of four fCO₂ products, shown also as individual data points.



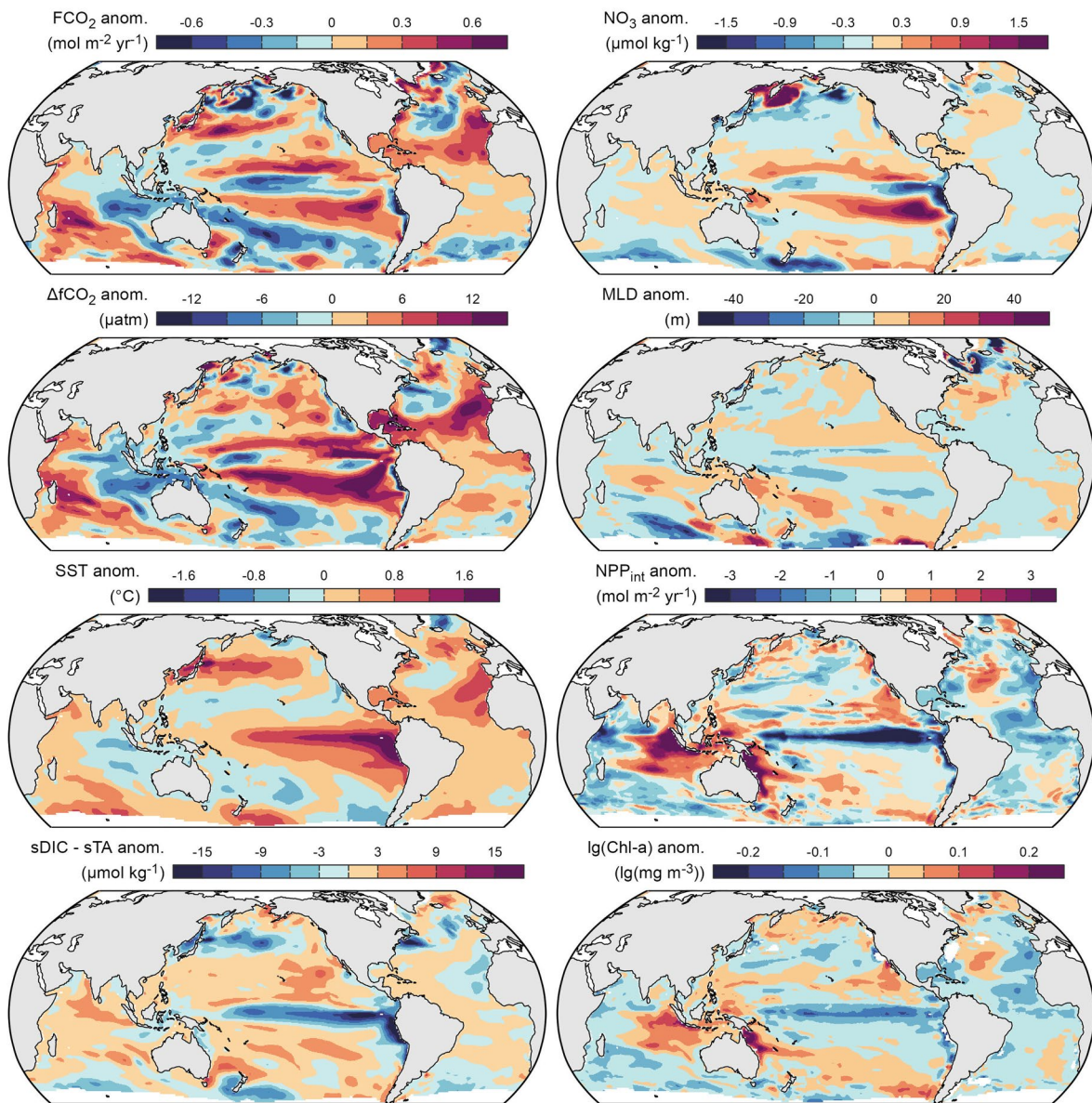
Extended Data Fig. 6 | Total annual mean $f\text{CO}_2$ anomalies (grey) in 2023 per ocean biome, decomposed into the thermal (red) and non-thermal (blue) anomaly components. Results are the same as in Fig. 3d-f, but shown

as biome means weighted by area and $k_w K_o$. Colored bars represent the mean, and uncertainty bars the standard deviation across the ensemble of four $f\text{CO}_2$ products, shown also as individual data points.



Extended Data Fig. 7 | Seasonal drivers and decomposition of $f\text{CO}_2$ anomalies.
 (a) Same as Fig. 4a and b, but showing the four $f\text{CO}_2$ products and two GOBMs individually. In addition to the three biomes in Fig. 4, estimates for the non-polar

global ocean are displayed. Furthermore, (b) the two main drivers of the flux anomalies and (c) the decomposition of the $f\text{CO}_2$ anomalies into their thermal and non-thermal components are shown.



Extended Data Fig. 8 | Annual mean surface anomaly maps of biogeochemical and physical variables in 2023. Anomaly estimates are based on the mean of two GOBM simulations.